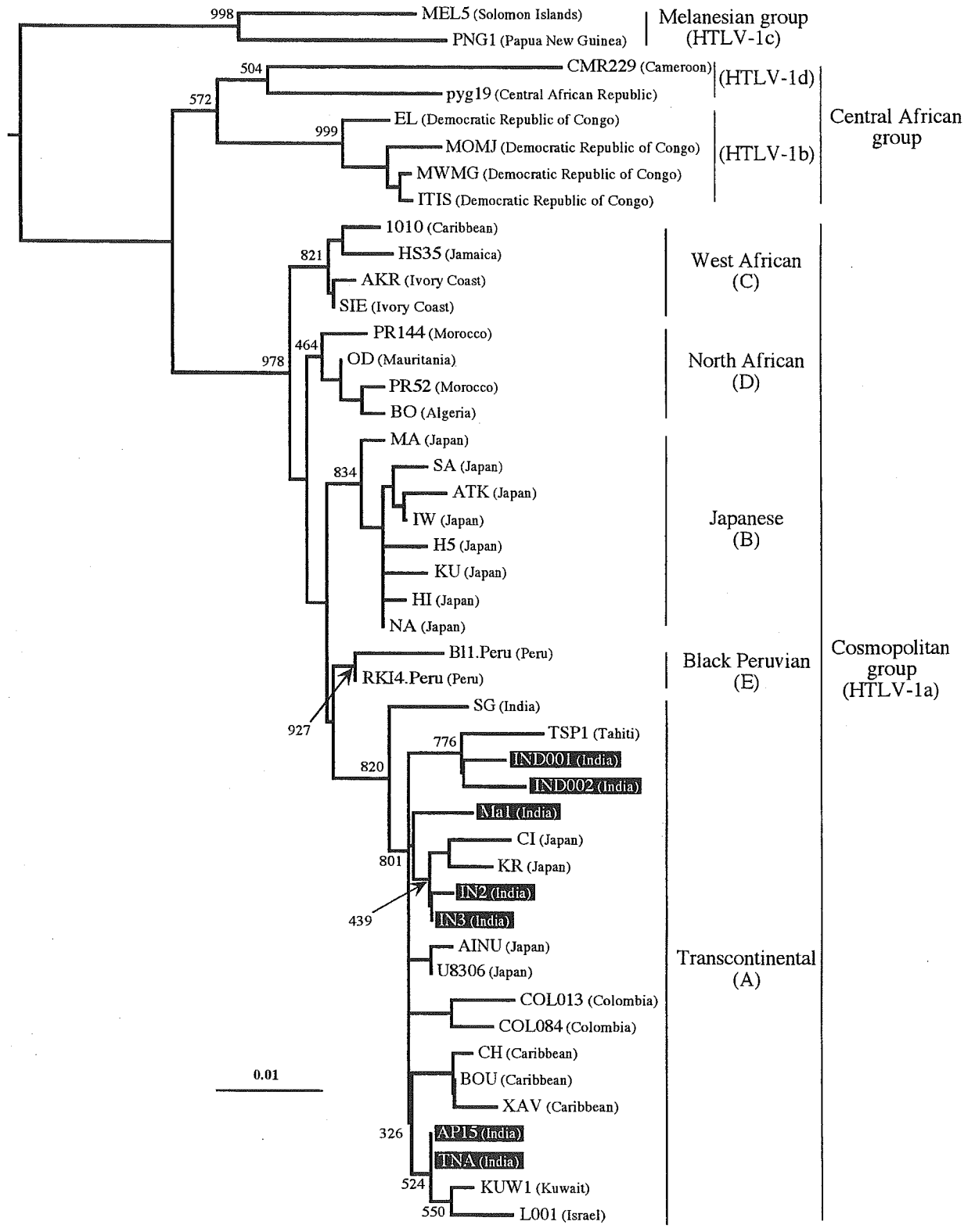

FIG. 1. Phylogenetic tree of HTLV-1 isolates based on a part of the LTR region (nucleotide positions 122–628 in ATK), showing the evolutionary relationships between the new isolates from India and isolates previously reported. Newly isolated HTLV-1s from India are highlighted. The tree was constructed by using the neighbor-joining (NJ) method. The scale at the bottom of the tree indicates the number of nucleotide substitutions per site. The horizontal branch lengths are proportional to the genetic distance. Numbers at nodes are bootstrap values. The tree was rooted with a prototype isolate of HTLV-2, MoT. The other DNA sequences used for construction of the phylogenetic tree have been described previously.[7]

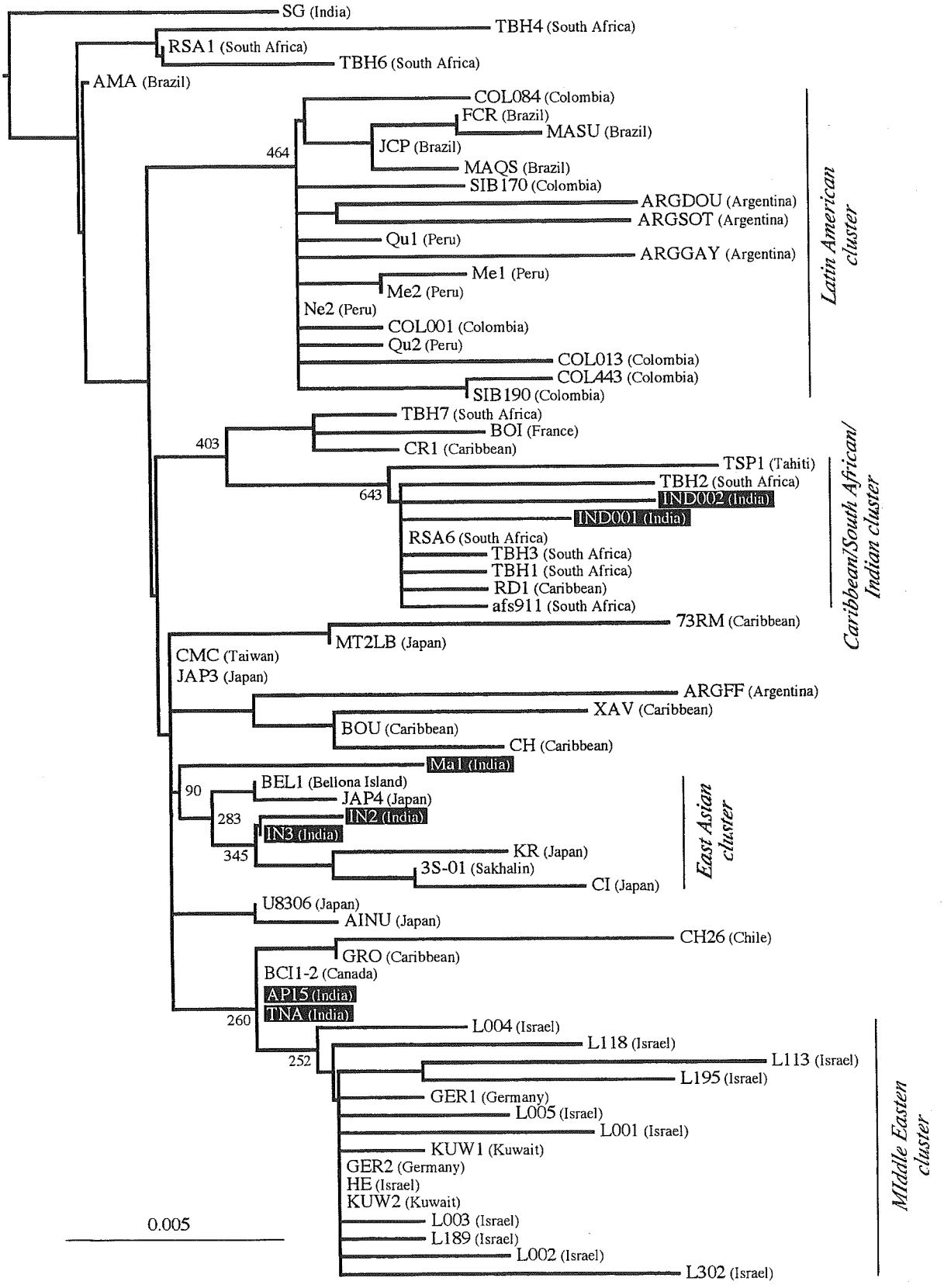

FIG. 2. Phylogenetic tree of HTLV-1 isolates that belong to subgroup A. The new isolates from India are boxed in black. The tree was constructed on the basis of a part of the LTR region (nucleotide positions 122–628 in ATK) by using the NJ method. The tree was rooted with strains of the Central African and Melanesian groups. For details, see the legend to Fig. 1.

ability of populations in the southern parts of India, where the Dravidians are the major inhabitants and HTLV-1 is highly prevalent.[10–12] The genetic diversity of the southern Indian populations was estimated to be as high as that of Africans and even higher than that of Europeans and other Asians based on sequence data of mitochondrial DNA and the allele frequency of several genetic loci.[13] Taken together, these findings imply that different lineages of the Dravidians carried different genotypes of subgroup A HTLV-1 when they reached India.

According to this scenario, some of the HTLV-1s in India could have been taken to other HTLV-1-prevalent areas such as the Middle East, South Africa, and the Caribbean basin. The genetic similarities between two of the new Indian isolates (AP15 and TNA) and the Middle Eastern isolates (Fig. 2), as well as the geographic proximity of India and the Middle East, strongly suggest movements of HTLV-1 carriers between these two areas, which is consistent with previous reports.[4] If this is the case, HTLV-1 might have been brought from India to the Middle East on the basis of the higher diversity among HTLV-1s in southern India than among Middle Eastern HTLV-1s (Fig. 2). Our results also show that two of the new isolates (IND001 and IND002) were phylogenetically related to South African and Caribbean HTLV-1s. This raises the possibility that some Indian HTLV-1s were introduced to South Africa and the Caribbean basin, as was previously proposed.[14] This possibility is consistent with the facts that more than a half million Indians migrated to the Caribbean basin as indentured laborers after the abolition of the trans-Atlantic slave trade in the early nineteenth century, and that South Africa served as a waystation during the migration.

After the putative introduction of Indian HTLV-1 to South Africa, some of the migrants may have gone back to India, possibly carrying human immunodeficiency virus type 1 (HIV-1). This is because the seropositivity against HTLV-1 among HIV-1 seropositives was significantly higher than that among HIV seronegatives in southern India.[11] This suggests that HTLV-1 was sexually transmitted among some HIV-1 seropositives in southern India. As Indian HIV likely originated from South Africa, some Indian HTLV-1s may have originated from the same place.

In summary, we speculate that Dravidian speakers originally carried HTLV-1 to southern India. This is supported by the following two points. First, the seven HTLV-1s isolated in southern India in this study are all in subgroup A and are highly heterogeneous. Second, India has the most divergent strain of subgroup A[9] (Fig. 1). Nonetheless, it is unclear how Dravidian speakers originally acquired HTLV-1. With respect to the origin of HTLV-1 of the Dravidians, it is interesting that the sickle cell gene haplotypes in southern India are the same as those in Africa,[15] and that the Dravidian languages have some similarities to those spoken in the Sahel Belt of Africa (from Sudan to Senegal).[16] It also remains unclear why HTLV-1s of Japan and South America are phylogenetically related to those of India. Future phylogenetic analyses of HTLV-1s in the Sahel Belt and South and Central Asia will help to identify the origin of Indian HTLV-1 and elucidate how it was disseminated in Asia.

ACKNOWLEDGMENT

This work was supported by a Grant-in-Aid from the Ministry of Education, Science, Sports, and Culture, Japan.

REFERENCES

1. Gessain A, Barin F, Vernant J, *et al.*: Antibodies to human T-lymphotropic virus type-I in patients with tropical spastic paraparesis. Lancet 1985;ii:407–409.
2. Hinuma Y, Nagata K, Hanaoka M, *et al.*: Adult T-cell leukemia: Antigen in an ATL cell line and detection of antibodies to the antigen in human sera. Proc Natl Acad Sci USA 1981;78:6476–6480.
3. Poiesz B, Ruscetti F, Gazdar A, *et al.*: Detection and isolation of type C retrovirus particles from fresh and cultured lymphocytes of a patient with cutaneous T-cell lymphoma. Proc Natl Acad Sci USA 1980;77:7415–7419.
4. Nerurkar V, Babe P, Song K, *et al.*: Sequence analysis of human T cell lymphotropic virus type I strains from southern India: Gene amplification and direct sequencing from whole blood blotted onto filter paper. J Gen Virol 1993;74:2799–2805.
5. Koyanagi Y, Yoshida T, Suzuki M, *et al.*: Dual infection of HIV-1 and HTLV-I in south India: A study on a patient with AIDS-related complex. Microbiol Immunol 1993;37:983–986.
6. Chandy M, Babu P, Saraswathi N, Ishida T, and John T: HTLV-I infection in patients with leukaemia in southern India. Lancet 1991;338:380–381.
7. Ohkura S, Yamashita M, Cartier L, *et al.*: Identification and phylogenetic characterization of a human T-cell leukaemia virus type I isolate from a native inhabitant (Rapa Nui) of Easter Island. J Gen Virol 1999;80:1995–2001.
8. Hashimoto K, Lalkaka J, Fujisawa J, *et al.*: Limited sequence divergence of HTLV-I of Indian HAM/TSP patients from a prototype Japanese isolate. AIDS Res Hum Retroviruses 1993;9: 495–498.
9. Miura T, Fukunaga T, Igarashi T, *et al.*: Phylogenetic subtypes of human T-lymphotropic virus type I and their relations to anthropological background. Proc Natl Acad Sci USA 1994;91:1124–1127.
10. Roy M, Das MK, Ishida T, *et al.*: Absence of HTLV-I infection in some Indian populations. Indian J Med Res 1994;100:160–162.
11. Babu P, Ishida T, Nesadoss J, and John T: Prevalence of HTLV-I/II antibodies in HIV seropositive and HIV seronegative STD patients in Vellore region in southern India. Scand J Infect Dis 1995;27:105–108.
12. Kelkar R, Ishida T, Bharucha Z, Advani SH, and Hayami M: Seroepidemiological survey of HTLV-I in blood donors in India. Indian J Haematol 1990;8:11–14.
13. Majumder PP: People of India: Biological diversity and affinities. Evol Anthropol 1998;6:100–110.
14. Song K, Nerurkar V, Pereira-Cortez A, *et al.*: Sequence and phylogenetic analyses of human T cell lymphotropic virus type I from a Brazilian woman with adult T cell leukemia: Comparison with virus strains from South America and the Caribbean basin. Am J Trop Med Hyg 1995;52:101–108.
15. Niranjan Y, Chandak GR, Veerraju P, and Singh L: Some atypical and rare sickle cell gene haplotypes in populations of Andhra Pradesh, India. Hum Biol 1999;71:333–340.
16. Koenraad E: Some new arguments. In: *Update on the Aryan Invasion Debate*. Aditya Prakashan, Delhi, India, 1999, pp. 238–320.

Address reprint requests to:
Masanori Hayami
Laboratory of Primate Model
Experimental Research Center for Infectious Diseases
Institute for Virus Research
Kyoto University
Kyoto 606-8507, Japan

E-mail: mhayami@virus.kyoto-u.ac.jp

J. Biochem. **138**, 583–592 (2005)
doi:10.1093/jb/mvi158

Solution RNA Structures of the HIV-1 Dimerization Initiation Site in the Kissing-Loop and Extended-Duplex Dimers

Seiki Baba[1], Ken-ichi Takahashi[1,2], Satoko Noguchi[1], Hiroshi Takaku[1], Yoshio Koyanagi[3], Naoki Yamamoto[4] and Gota Kawai[1,*]

[1]Department of Life and Environmental Sciences, Chiba Institute of Technology, 2-17-1 Tsudanuma, Narashino, Chiba 275-0016; [2]Department of Bioscience, Faculty of Bioscience, Nagahama Institute of Bio-Science and Technology, 1266 Tamura-cho, Nagahama, Shiga 526-0829; [3]Institute for Virus Research, Kyoto University, Kyoto 606-8507; and [4]AIDS Research Center, The National Institute of Infectious Diseases, Toyama 1-23-1, Shinjuku-ku, Tokyo 162-8640

Received April 27, 2005; accepted August 13, 2005

Dimer formation of HIV-1 genomic RNA through its dimerization initiation site (DIS) is crucial to maintaining infectivity. Two types of dimers, the initially generated kissing-loop dimer and the subsequent product of the extended-duplex dimer, are formed in the stem-bulge-stem region with a loop including a self-complementary sequence. NMR chemical shift analysis of a 39mer RNA corresponding to DIS, DIS39, in the kissing-loop and extended-duplex dimers revealed that the three dimensional structures of the stem-bulge-stem region are extremely similar between the two types of dimers. Therefore, we designed two shorter RNA molecules, loop25 and bulge34, corresponding to the loop-stem region and the stem-bulge-stem region of DIS39, respectively. Based upon the chemical shift analysis, the conformation of the loop region of loop25 is identical to that of DIS39 for each of the two types of dimers. The conformation of bulge34 was also found to be the same as that of the corresponding region of DIS39. Thus, we determined the solution structures of loop25 in each of the two types of dimers as well as that of bulge34. Finally, the solution structures of DIS39 in the kissing-loop and extended-duplex dimers were determined by combining the parts of the structures. The solution structures of the two types of dimers were similar to each other in general with a difference found only in the A16 residue. The elucidation of the structures of DIS39 is important to understanding the molecular mechanism of the conformational dynamics of viral RNA molecules.

Key words: DIS, HIV-1, NMR, RNA, structure.

Abbreviations: DIS, dimerization initiation site; HIV-1, human immunodeficiency virus type 1.

Two molecules of viral genomic RNA are packaged in a dimeric state in the virion of human immunodeficiency virus type 1 (HIV-1), and this dimer formation is crucial to maintaining their infectivity (*1–4*). Accumulating evidence from both *in vivo* and *in vitro* experiments has shown that the specific sequence, the dimerization initiation site (DIS) located close to the 5′ terminus of the genomic RNA, is required for spontaneous dimerization of HIV-1 RNA. DIS can form a stem-loop structure with a self-complementary sequence in the loop and a bulge in the stem (*5, 6*). The dimerization of DIS forms the kissing-loop dimer as the first step; then, their intramolecular stems are converted into intermolecular stems, generating the extended-duplex dimer (*7, 8*). This two step dimerization process is called the kissing-loop mechanism. The kissing-loop dimer is converted into the extended-duplex dimer by incubation at 55°C (*9, 10*) or by incubation at physiological temperature with the HIV-1 nucleocapsid protein, NCp7, which includes two basic regions and two zinc-fingers (*11*). A number of experiments have been performed to gain an understanding of the role of the zinc-fingers as well as the basic regions (*12–16*). Our previous results show that, for the two step dimerization from the kissing-loop dimer to the extended-duplex dimer, the two basic regions surrounding the N-terminal zinc finger of NCp7 have RNA chaperone activity by themselves, and the zinc fingers increase the efficiency of the activity (*17, 18*).

A number of three dimensional structural analyses using NMR and X-ray methods have been performed to determine the conformation of each region of DIS, the loop region in the kissing-loop (*19, 20*) or extended-duplex dimers (*21–24*), as well as the bulge-out region (*25–27*). However, our previous studies suggested that the 39mer RNA sequence, DIS39, which covers the entire bulge and loop regions, is necessary and sufficient for the two step dimerization (*28, 29*). Thus, it is still relevant to determine the structures of the kissing-loop and extended-duplex dimers for DIS39 with the same sequence and conditions.

In the present study, we designed two shorter RNA molecules, loop25 and bulge34; loop25 includes the loop-stem region of DIS39, and bulge34 includes the stem-bulge-stem region (Fig. 1), respectively we then determined the solution structures of loop25 in each of the kissing-loop and extended-duplex dimers as well as bulge34. By combining the structure parts, the solution structures of DIS39 in the kissing-loop and extended-duplex dimers were able to be determined.

*To whom correspondence should be addressed. Tel/Fax: +81-47-478-0425, E-mail: gkawai@sea.it-chiba.ac.jp

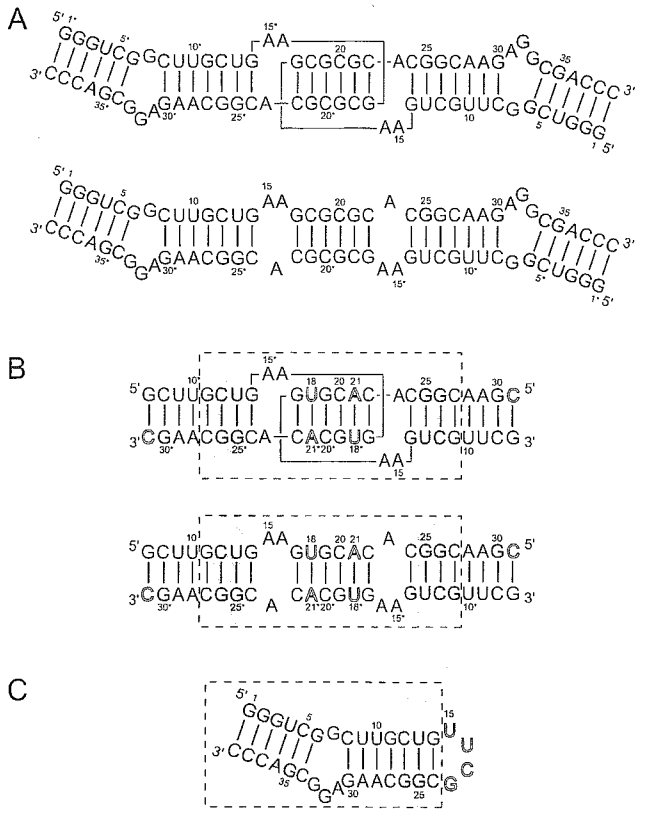

Fig. 1. **Secondary structure of a 39mer RNA corresponding to the dimerization initiation site (DIS39) and its fragments used in this study.** (A) The kissing-loop and extended-duplex dimers of DIS39. (B) The kissing-loop and extended-duplex dimers of loop25, which is composed of the loop and stem of DIS39. Modified residues are indicated by open characters. The sequence of the self-complementary loop was modified to increase the dispersion of NMR signals, and a base pair was added to the stem. The broken box indicates the part to be used for structure calculation. (C) Bulge34 consists of the stem-bulge-stem region of DIS39 and the connecting UUCG loop. The broken box indicates the part to be used for structure calculation. Gray shading indicates the two base pairs, C12–G26 and U13–G25, that are superimposed to combine the structures of the kissing-loop or extended-duplex dimer region and the stem-bulge-stem region. Asterisks indicate residues in the other strand.

MATERIALS AND METHODS

RNA Synthesis, Purification and Preparation—Nonlabeled loop25 was synthesized chemically by the phosphoramidite method with an automatic DNA/RNA synthesizer, Expedite model 8909 (PerSeptive Biosystems Inc., MA, USA). The protection groups were removed with ammonia and tetra-*n*-butylammonium fluoride. Nonlabeled DIS39 and bulge34 were synthesized enzymatically by the *in vitro* transcription reaction method with AmpliScribe T7 transcription kits (Epicentre Technologies Co., WI, USA). Purification for each RNA sample was performed by PAGE using 30 cm × 40 cm glass plates (Nihon Eido Co. Ltd., Tokyo, Japan) under denaturing conditions, and extensive desalting by ultrafiltration (Centricon YM3, Amicon Inc., MA, USA) was carried out. For stable isotopic labeling by the *in vitro* transcription with ^{13}C- and ^{15}N-labeled NTPs (Nippon Sanso, Tokyo, Japan), we used DIS39 rather than shorter loop25 and bulge34 because the efficiency of *in vitro* transcription is better for larger RNA.

For the preparation of the kissing-loop dimer, DIS39 or loop25 in water was incubated at 368 K for 5 min and chilled on ice for 5 min. Then, the solvent was adjusted to 1× PN-buffer [10 mM sodium phosphate (pH 7.0) and 50 mM NaCl] by adding concentrated buffer. For the preparation of the extended-duplex dimer, DIS39 or loop25 in 1× PN-buffer was incubated at 368 K for 5 min and slowly cooled to room temperature. Bulge34 was annealed by heating at 363 K for 5 min and snap-cooling on ice. To confirm the formation of the hairpin structure, the samples were subjected to a native PAGE experiment. For NMR measurements, RNA samples were dissolved in 10 mM sodium phosphate buffer (pH 7.0) containing 50 mM NaCl. The final concentration of chemically synthesized loop25 was 1.8 mM. The concentrations of DIS39 and bulge34 (transcripts) were 1.0 and 0.5 mM, respectively. The concentration of the kissing-loop and extended-duplex dimers of [G-^{13}C/^{15}N] and [A-^{13}C/^{15}N] DIS39 were 0.4, 0.3, 0.2 and 0.1 mM, respectively.

NMR Measurements—NMR spectra were recorded on Bruker DRX-500 and DRX-600 spectrometers. Spectra were recorded at probe temperatures of 283 to 303 K and NMR data at 298 K were used for structure calculation. The imino proton signal of the G and U residues in H_2O were distinguished from each other by the HSQC selected and HSQC filtered 1D spectra measured with ^{13}C and ^{15}N-labeled DIS39. Exchangeable proton NOEs were determined by 2D NOESY in H_2O with a mixing time of 150 ms using the jump-and-return scheme and gradient pulses for water suppression. For resonance assignments, well-established procedures were used (*30*). The H2 protons of adenosine were assigned based on a 2D HSQC experiment with natural abundance ^{13}C. NOE distance restraints from non-exchangeable protons were obtained from 2D NOESY experiments (mixing times of 50, 100, 200, and 400 ms) in D_2O. The intensities of the NOEs between exchangeable protons were interpreted as distances of 2.1–5.0 Å. For loop25, distances were estimated by analyzing the initial slope of NOE intensities for mixing times of 25, 50, 100, 200 ms. Judgment of intermolecular NOE is described in the result section. Two restraints (>5 Å) were added to the distance restraints based on the absence of NOE cross peaks in the case of the kissing-loop dimer. For bulge34, the intensities of NOEs due to nonexchangeable protons were interpreted as distances with a margin of −1.5 to +1.5 Å for the 100 ms 2D NOESY and −1.0 to +2.0 Å for the 200 ms 2D NOESY. Two restraints (>5 Å) were added to the distance restraints based on the absence of NOE cross peaks. The formation of hydrogen binding of G:C, A:U or G:U base pairs is interpreted as distance constraints as 1.8–2.1 Å for hydrogen and acceptor atoms and 2.8–3.2 Å for donor and acceptor atoms; G11:C27 to G14:C24, G11*:C27* to G14*:C24* and G17:C22* to C22:G17* for loop25 in the kissing-loop dimer, G11:C27* to G14:C24*, G11*:C27 to G14*:C24 and G17:C22* to C22:G17* for loop25 in the extended-duplex dimer, and G1:C39 to C5:G35 and U9:A29 to G14:C24 for bulge34. Dihedral restraints were obtained as described below. The absence of crosspeaks between H1′–H2′ in the 2D TOCSY and DQF-COSY experiments was interpreted as the residue being in the C3′-*endo*

conformation. On the other hand, the presence of strong crosspeaks between H1′–H2′ in the 2D TOCSY and DQF-COSY experiments was interpreted as the residue being in the C2′-*endo* conformation. The correction of sugar puckering is interpreted as dihedral restraints for ν_2 as 40.00 ± 20.00° (C3′-*endo*) or −35.00 ± 20.00° (C2′-*endo*). Based on the sequential connectivity of the Watson-Crick and G-U base pairs, the RNA-A conformation was assumed for the stem region and dihedral restraints were introduced for backbone torsion angles (α, β, γ, δ, ε and ζ) as the ideal conformation with a margin of ±10.00°. For loop25 in the kissing-loop dimer, information about the C3′-*endo* conformation (G11–G14, G17–C27), the C2′-*endo* conformation (A16) and RNA-A conformation in the stem region (G11–U13, U18–A21, G25–C27) was used as the dihedral restraints. For loop25 of the extended-duplex dimer, information about the C3′-*endo* conformation (G11–G14, G17-C27) and RNA-A conformation in the stem region (G11–U13, U18–A21, G25–C27) was used as the dihedral restraints. For bulge34, the information about the C3′-*endo* conformation (G1–G14, C24–A31, C34–C39) and RNA-A conformation in the stem region (G1–C5, G11–G14, C24–C27, G35–C39) was used as the dihedral restraints.

Structure Calculation—A set of 100 structures was calculated using the simulated annealing protocol described below with the InsightII/Discover package, and the amber force field was used. The force constants were 100 kcal mol^{-1} $Å^{-2}$ for distance restraints and 100 kcal mol^{-1} rad^{-2} for dihedral restraints. The starting coordinates were randomized, and the randomized structures were heated to 2,000 K in 5 ps, and the temperature was kept to 2,000 K for another 5 ps. After that, all restraints were increased to full values in 20 ps, then, decreased to 1/10 of full values in 5 ps at 2,000 K. Van der Waals radii were increased from 0.1 to 0.825 in 20 ps at 2,000 K. All restraints were increased to full value again in 10 ps at 2,000 K. Scalings for non-bond interactions were increased to full value in the next 20 ps at 2,000 K, and the temperature was kept to 2,000 K for another 5 ps. Then, the temperature was gradually scaled to 300 K in 10 ps. After that, the structure was heated from 300 to 1,000 K in 5 ps, and the van der Waals radii were increased from 0.825 to 1 at 1,000 K, and then decreased from 1 to 0.825 at 1,000 K. An additional 5 ps of dynamics was performed at 1,000 K, and the temperature was gradually scaled to 300 K for 10 ps. A final minimization step was performed, which included a Lennard-Jones potential and electrostatic terms with a dielectric constant of 7. The ten final structures with the lowest total energies were chosen.

RESULTS AND DISCUSSION

Analysis of the NMR Spectra of DIS39, Loop25 and Bulge34—Our previous NMR study revealed that the two types of dimers of DIS39 prepared as described in "MATERIALS AND METHODS" correspond to the kissing-loop and extended-duplex dimers (*31*). NMR spectra of DIS39 in each of the kissing-loop and extended-duplex dimers were measured in D_2O, and the signals due to H1′, H6/H8 were assigned by the sequential assignment method (Fig. 2). Figure 3A shows the difference in the chemical shift of H1′, H6/H8 between the two types of dimers. It was found that the difference is concentrated in the loop region. Interestingly, structures of the stem-bulge-stem region of the kissing-loop and extended-duplex dimers were extremely similar, even though the stems are formed by intra and inter molecules. This was also shown by analysis of the TOCSY spectrum; differences are located in the loop regions. Most residues were adapted to the C3′-*endo* conformation except for G32, G33 in the bulge-out region of both forms, A16 in the kissing-loop dimer and A15, A16 in the extended-duplex dimer, which might be a mixture of the C2′-*endo* and C3′-*endo* conformations.

To reveal further authentic structure, two RNA molecules were designed; loop25 includes the loop region and bulge34 includes the stem-bulge-stem region (Fig. 1, B and C). Loop25 was constructed to determine the authentic structure of the loop region. In order to increase the dispersion of the NMR signals, the sequence of the loop was modified from GCGCGC to GUGCAC. One base pair was added by replacing A31 by C31 in the stem to increase the stability of the kissing-loop dimer. It is noted that the loop sequences of GCGCGC and GUGCAC correspond to those of HIV-1 subtypes B and F (*32*), respectively, and both sequences have dimerization activity (*6*, *9*, *10*). The chemical shifts of loop25 were compared with those of DIS39 in each of the kissing-loop and extended-duplex dimers (Fig. 3, B and C). For both conformations, the chemical shifts for most of the stem region and A15, A16 and A23 were strikingly similar between the loop25 and DIS39. Due to the base alterations, the chemical shifts of the self complement loop were slightly different for both dimers. The chemical shift of H8 was shifted more than 0.2 ppm due to the addition of the terminal base pair. It is noteworthy that the chemical shift difference in loop25 between the kissing-loop and extended-duplex dimers (Fig. 3D) was almost identical to that of DIS39 (Fig. 3A). These results indicate that the structures of loop25 in the kissing-loop and extended-duplex dimers are essentially identical to those of DIS39. Upon analysis of the TOCSY spectrum, it was found that most of the residues were adapted to the C3′-*endo* conformation except A15 and A16 for the extended duplex dimer and A16 for the kissing loop dimer, and these results also agree with the results for DIS39.

Bulge34 was constructed to determine the authentic structure of the stem-bulge-stem region. Bulge34 consists of the stem-bulge-stem region of DIS39 and the connecting UUCG loop. The NMR signals of bulge34 were assigned by the sequential assignment technique. The chemical shift of H1′, H6/H8 of bulge34 were compared to those of DIS39 in the kissing-loop dimer (Fig. 3E). The chemical shifts for the stem-bulge-stem regions of bulge34 and DIS39 were identical, although the chemical shifts of the residues adjacent to the loop were slightly different by reflecting the difference in the closing loop sequences. Upon analysis of the TOCSY spectrum, it was found that most residues were adapted to the C3′-*endo* conformation except for G32, G33 in the bulge-out region and C in the UUCG loop, and that the conformation in the stem-bulge-stem region also agreed with that of DIS39. These results indicate that the structure of the stem-bulge-stem region of bulge34 is identical to that of DIS39.

Thus, the structures of DIS39 for two types of dimers can be determined by determining the structures of loop25 and bulge34, and combining them.

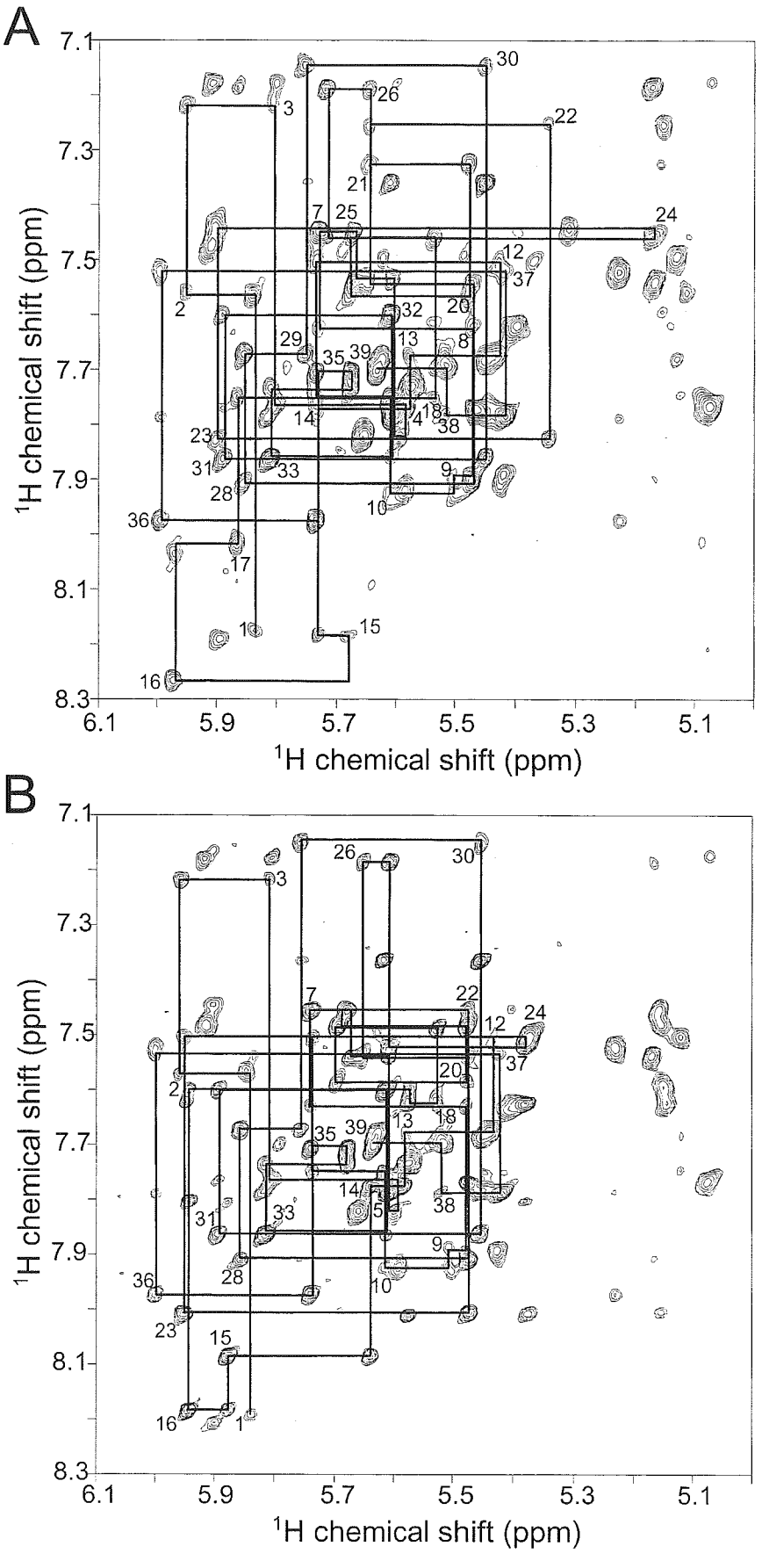

Fig. 2. **2D NOESY spectra of the (A) kissing-loop and (B) extended-duplex dimers of DIS39 measured in D_2O at 25°C with a mixing time of 200 ms.** Cross-peaks between aromatic H6/H8 protons and ribose H1′ protons are shown, and the sequential NOE connectivity is indicated.

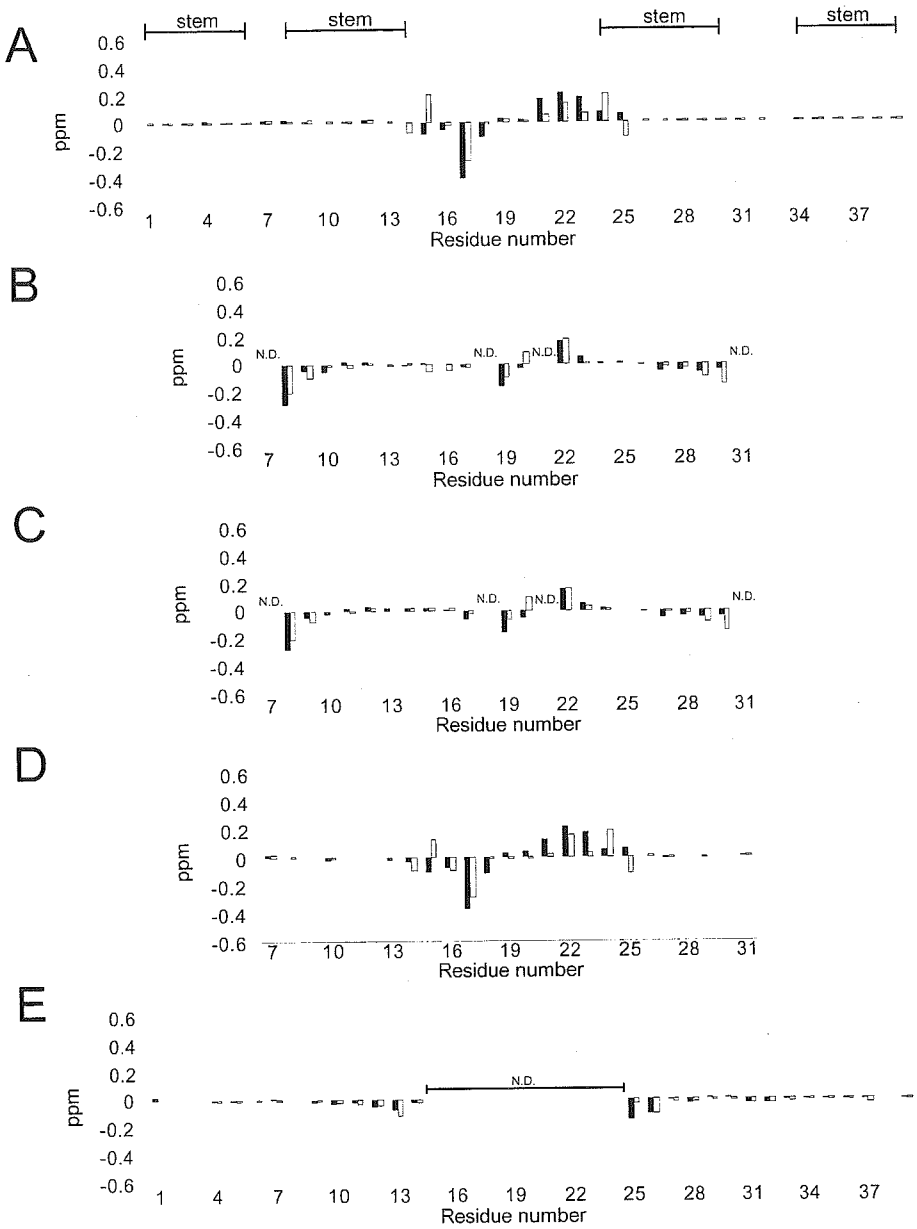

Fig. 3. **Chemical shift differences for H6/H8 and H1′.** Filled and open bars indicate H6/H8 and H1′, respectively. (A) Chemical shift differences between the kissing-loop and extended-duplex dimers of DIS39. Lines above the graph indicate the stem regions. (B) Chemical shift differences between DIS39 and loop25 in the kissing-loop dimer (data for replaced residues 7, 18, 21 and 31 are not shown). (C) Chemical shift differences between DIS39 and loop25 in the extended-duplex dimer (data for replaced residues 7, 18, 21 and 31 are not shown). (D) Chemical shift differences between the kissing-loop and extended-duplex dimers of loop25. (E) Chemical shift differences between DIS39 and bulge34 in the kissing-loop dimer (data for residues 15–24 are not shown).

Structure Determination—The loop region of loop25 in the kissing-loop dimer: To determine the structure of the loop region of DIS39 in both the kissing-loop and extended-duplex dimers, the NMR signals of loop25 were further analyzed and structural information was collected. The structure of the loop region consisting of the nine nucleotide loop and the stem with four base pairs was determined as shown by the broken box in Fig. 1B. A total of 286 distance restraints, 76 hydrogen bonding distance restraints, 140 dihedral restraints (Table 1), and 136 chiral restraints were used for the structural calculation. Three NOEs in the loop region, H2(A21)–H1′(U18), H2(A21)–H1′(G19) and H2(A21)–H8(G19), were judged to be intermolecular by analysis of the imino proton spectra. Four NOEs in the stem-loop linking region were considered to be intermolecular or intramolecular based on the results of the isotope filter NMR measurement (data not shown), and it was concluded that two NOEs, H2(A23)–H1′ (G17), H2(A16)–H1′ (G16), are intermolecular and three NOE, H8(A16)–H1′ (A16), H8(A16)–H2′ (A16), are intramolecular. One NOE in the stem-loop linking region was considered to be intermolecular or intramolecular in the structure calculation, and it was concluded that this NOE, H2(A23)–H2(A15), is intramolecular. Each restraint is used twice for two molecules. The structures were calculated by the restrained molecular dynamic calculation with the simulated annealing method. The structure was defined with a heavy atom r.m.s.d. of 2.14 Å for the ten converged structures (Fig. 4A, left panel), and the minimized average structure is shown in Fig. 4A (right panel). Although the overall convergence was not very good, the self-complementary region was well defined with 0.76 Å, and the stem-loop linking region was defined with 1.86 Å. The structural statistics are summarized in Table 1.

The loop region of loop25 in the extended-duplex dimer: The loop region of loop25 in the extended-duplex dimer was

Table 1. **NMR restraints and structural statistics.**

	Number of restraints		
	loop25 in the kissing-loop dimer (17 mer × 2)	loop25 in the extended-duplex dimer (17 mer × 2)	bulge34 (30 mer)
Distance restraints	286	384	345
imino-imino	12	12	10
intra residue	154	182	163
intra molecule	106	174	170
inter molecule	12	16	–
>5 Å	2	0	2
Hydrogen bonding distance restraints	76	76	58
Dihedral restraints	140	138	126
3′-*endo*	30	30	28
2′-*endo*	2	0	0
RNA-A stems	108	108	98
r.m.s.d. from the idealized geometry (Å)			
Bonds (Å)	0.00897 ± 0.00004	0.00803 ± 0.00020	0.00775 ± 0.00015
Angle (°)	2.43 ± 0.23	2.33 ± 0.05	2.24 ± 0.07
Impropers (°)	1.57 ± 0.10	1.82 ± 0.64	1.53 ± 0.21
Heavy-atoms r.m.s.d. (Å)[a]			
All	2.14	1.45	1.98
Stem-loop linking region[b]	1.86	1.31	
Bulge region[c]			1.90

[a]Averaged r.m.s.d. between an average structure and the 10 converged structures were calculated. The converged structures did not contain experimental distance violations >0.2 Å or dihedral violations >5°, [b]The stem-loop linking region consists of residues 14 to 17, 22 to 24, 14* to 17* and 22* to 24*, [c]The bulge region consists of residues 6 to 10 and 28 to 34. Asterisks indicate residues in the other molecule.

determined (broken box in Fig. 1B). A total of 384 distance restraints, 76 hydrogen bonding distance restraints, 138 dihedral restraints (Table 1) and 136 chiral restraints were used for the structure calculation. For the stem-loop linking region, H2 of A23 was connected by intermolecular NOEs to H1′ and H2 of A15, H2 of A16 and H1′ of G17. The structures were calculated by the restrained molecular dynamic calculation with the simulated annealing method described above. The structure was well defined with a heavy atom r.m.s.d. of 1.45 for the ten converged structures (Fig. 4B, left panel), and the minimized average structure is shown in Fig. 4B (right panel). The stem-loop linking region was defined with 1.31 Å. The structural statistics are summarized in Table 1.

The stem-bulge-stem region of bulge34: A structural determination was performed for bulge34 except for the UUCG loop (broken box in Fig. 1C). A total of 345 distance restraints, 58 hydrogen bonding distance restraints, 126 dihedral restraints (Table 1) and 120 chiral restraints were used for the structure calculation. Two NOE restraints (>5 Å), H2(A31)–H1′(U9) and H1′(A31)–H1′(U9), were added to the distance restraints based on the absence of NOE cross peaks. The structures were calculated by the restrained molecular dynamic calculation with a simulated annealing protocol. The structure was defined with a heavy atom r.m.s.d. of 1.98 for the ten converged structures (Fig. 4C, left panel), and the minimized average structure is shown in Fig. 4C (right panel). Although the overall convergence is not very good, the stem regions are well defined with 0.83 or 0.78 Å, respectively. The bulge region was defined with 1.90 Å. The structural statistics are summarized in Table 1.

The two types of dimers of DIS39: Solution structures of DIS39 were then constructed by combining the structure parts. The structures of the kissing-loop or extended-duplex dimer region and stem-bulge-stem region were combined by superimposing two base pairs, C12:G26 and U13:G25 (Fig. 1, gray area). The left panels of Fig. 5 show the ten structures prepared by using the minimized average structure of the stem-bulge-stem region (Fig. 4C, right) and each of the ten lowest energy structures of the loop region (Fig. 4, A or B, left) superimposed by the loop region. The right panels of Fig. 5 show the structures prepared using the minimized average structure of the stem-bulge-stem region (Fig. 4C, right) and the loop region (Fig. 4, A or B, right). The relative angles between the stem-bulge-stem regions differ between the kissing-loop and extended-duplex dimers as shown in the right panels of Fig. 5. However, the fluctuations of the relative angles are rather large and the ranges overlap between the two dimers as shown in the left panels of Fig. 5. In fact, the values of the residual dipolar coupling for the stem-bulge-stem region are similar between the kissing-loop and extended-duplex dimers (to be published). A preliminary normal mode analysis suggested the existence of hinge motion, and, in order to reveal the dynamic properties of the dimers, a molecular dynamics analysis, as well as the thermodynamics analysis (*33*), is required. The most obvious local difference was observed for A16; for the kissing-loop dimer, A16 was close to the same residue in the other molecule (Fig. 6A, left) and did not stack above A15 of the same molecule nor G17 of the other molecule (Fig. 6A, right), whereas for the extended-duplex dimer, A16 was apart from the same residue of the other molecule (Fig. 6B, left) and stacked between A15 and G17 (Fig. 6B, right).

Structural Comparison with Related Structures—Ennifar *et al.* (*20*) determined the crystal structure of

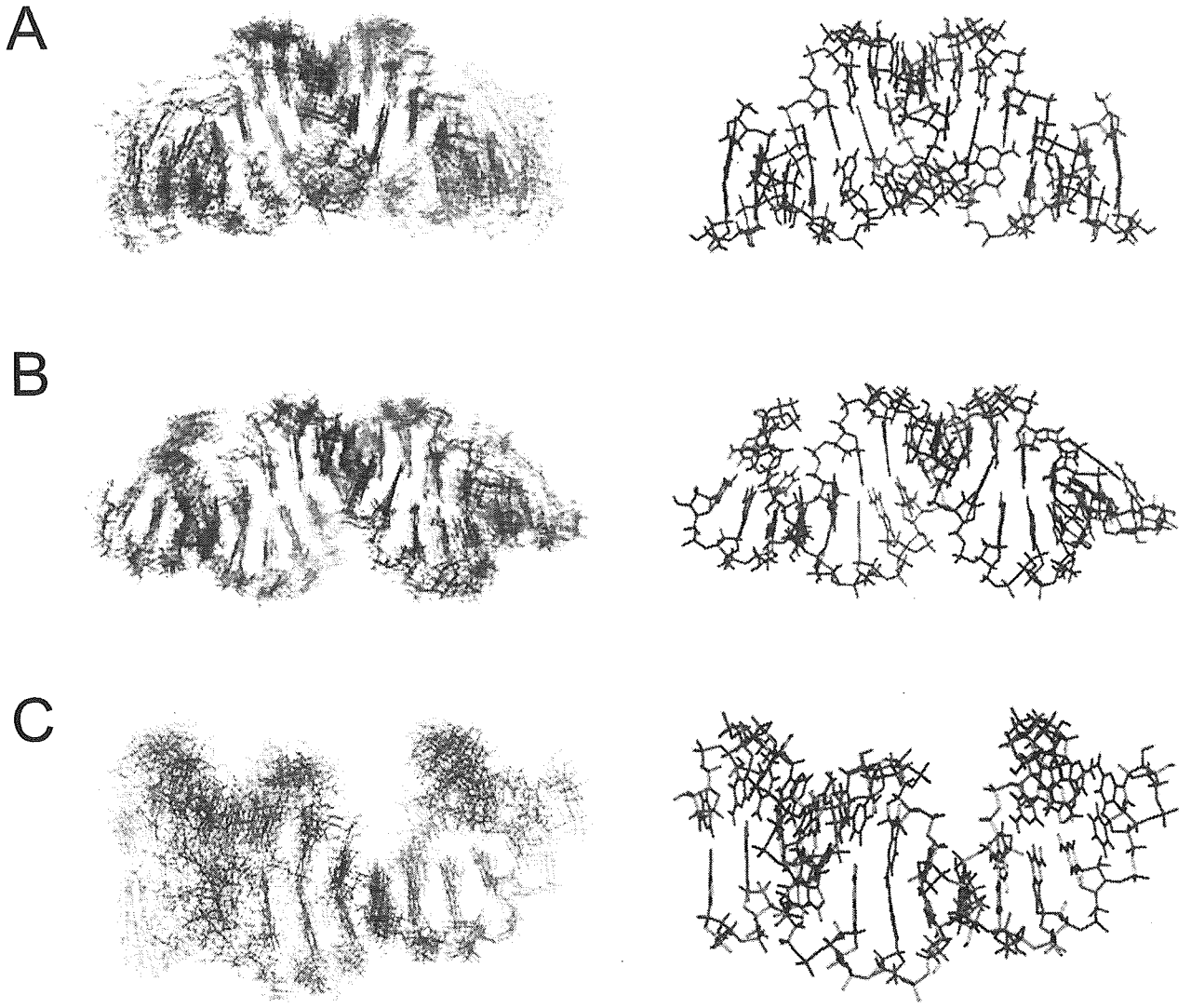

Fig. 4. **Solution structures of each part of DIS39.** Left panels show the superimposition of the 10 lowest energy structures and the right panels show the minimized average structures. (A) The loop region of loop25, as shown by the broken box in Fig. 1b, in the kissing-loop dimer. Each strand is colored in red or blue. (B) The loop region of loop25 in the extended-duplex dimer. (C) The stem-bulge-stem region of bulge34.

the kissing-loop dimer. The present structure is similar to the crystal structures in general, except for A15 and A16. In the present structure, A15 stacks on G14 and A16 interacts with the same residue in the other molecule (Fig. 6A, right). On the other hand, in the crystal structure, A15 and G16 are flipped out (*20*). It is noted that the numbering system of DIS39 is used for other structures for convenience, and position 16 is occupied by A or G depending on the strain. A15 and A16 (or G16) might be flexible and can be flipped out even in solution. Mujeeb *et al.* (*19*) determined the solution structure of the kissing-loop dimer. In this structure, A16 interacts with A15 and C24 in the other molecule, and, as a result, the distance between the two stems is relatively short. Thus, this restricted interaction makes the global structure different from the present structure and the crystal structure. However, the location of A15 is similar in the two solution structures. The difference in the conformation of A16 between the two solution structures may reflect the difference in the sequence of the stem adjacent to the loop and/or in the sample condition, including the salt concentration. The NOE connectivity determined in the present study agrees in general with those of Dardel *et al.* who analyzed the structure of the stem-loop region in the kissing-loop dimer by NMR (*34*).

Girard *et al.* (*21*) and Mujeeb *et al.* (*22*) determined the solution structures of extended-duplex dimers. In these two structures, as well as in the present structure, A15, A16 and A23 form a zipper like structure (Fig. 6B, right). On the other hand, in the case of the crystal structure of the extended-duplex dimer, G16 forms a G:A base pair and A15 is flipped out, and it was assumed that this in-out bulge transconformation is magnesium-dependent (*23*).

Structures of the stem-bulge-stem region were shown by Lawrence *et al.* (*26*) and Yuan *et al.* (*27*). In the solution structure determined by Lawrence *et al.* (*26*), continuous stackings were formed for each strand, G6-C8 and

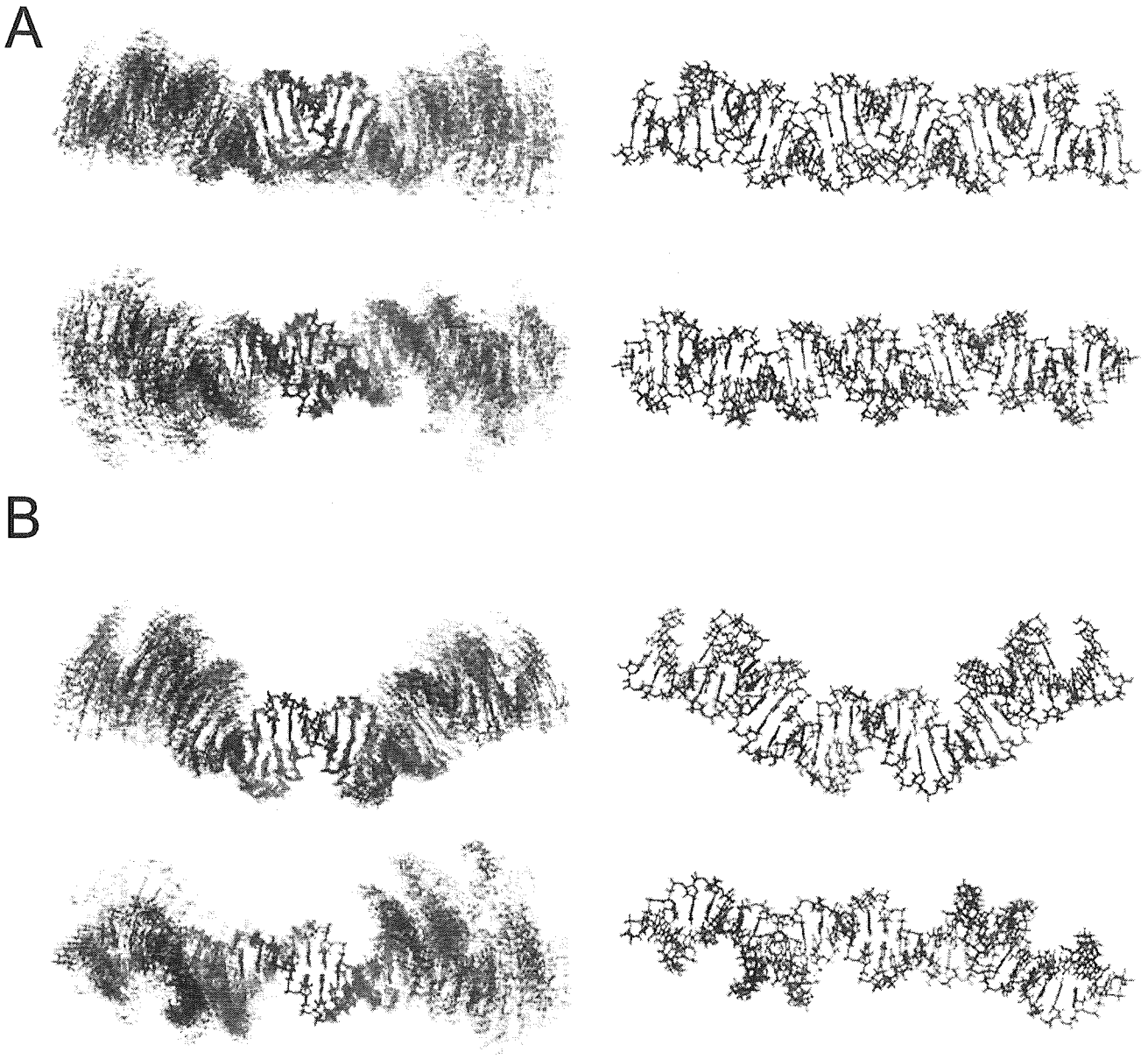

Fig. 5. **Solution structures of the (A) kissing-loop and (B) extended-duplex dimers of DIS39.** Left panels show the structures constructed by combining the structures of the loop (the 10 lowest energy structures of the kissing-loop or extended-duplex dimers) and the stem-bulge-stem (minimized average structure) regions. Right panels show the structures constructed by combining the minimized average structures of the loop and stem-bulge-stem regions. The two regions were combined by superimposing two base pairs, C12–G26 and U13–G25 (Fig. 1, gray area). Each strand is colored in red or blue and views from two different directions are shown.

G30-C34. Yuan *et al.* (*27*) showed that G7 and A31 form a base pair, and that G33 is not always stacked on G32 or C34, and, in general, the present structure is identical to the latter structure. Greatorex *et al.* (*25*) showed that the bulge region is too flexible to determine the conformation. These conformational differences may be caused by differences in the stability of the terminal stem. Lawrence *et al.* (*26*) adopted a stable 7 base-pair stem, and their structure forms an ordered conformation in the bulge region. In contrast, Greatorex *et al.* (*25*) adopted an unstable 4 base-pair stem and the bulge region is flexible. Yuan *et al.* (*27*) adopted a 4 base-pair stem and a flanking adenosine residue at the 3′ terminal that must stabilize the stem. In the present study, a 6 base-pair stem was used.

Mechanism of the Two Stem Dimerization—Between the kissing-loop and extended-duplex dimers, A16 shows the most drastic change in interaction with other residues, suggesting that A16 is the key residue in the two step dimerization reaction. The difference in the A16 conformation among structures with different sequences and determined under different conditions as described above, also suggests the importance of this residue. Mujeeb *et al.* (*19*, *22*) also pointed out the flexibility around the junction of the loop and the stem of DIS in the kissing-loop and

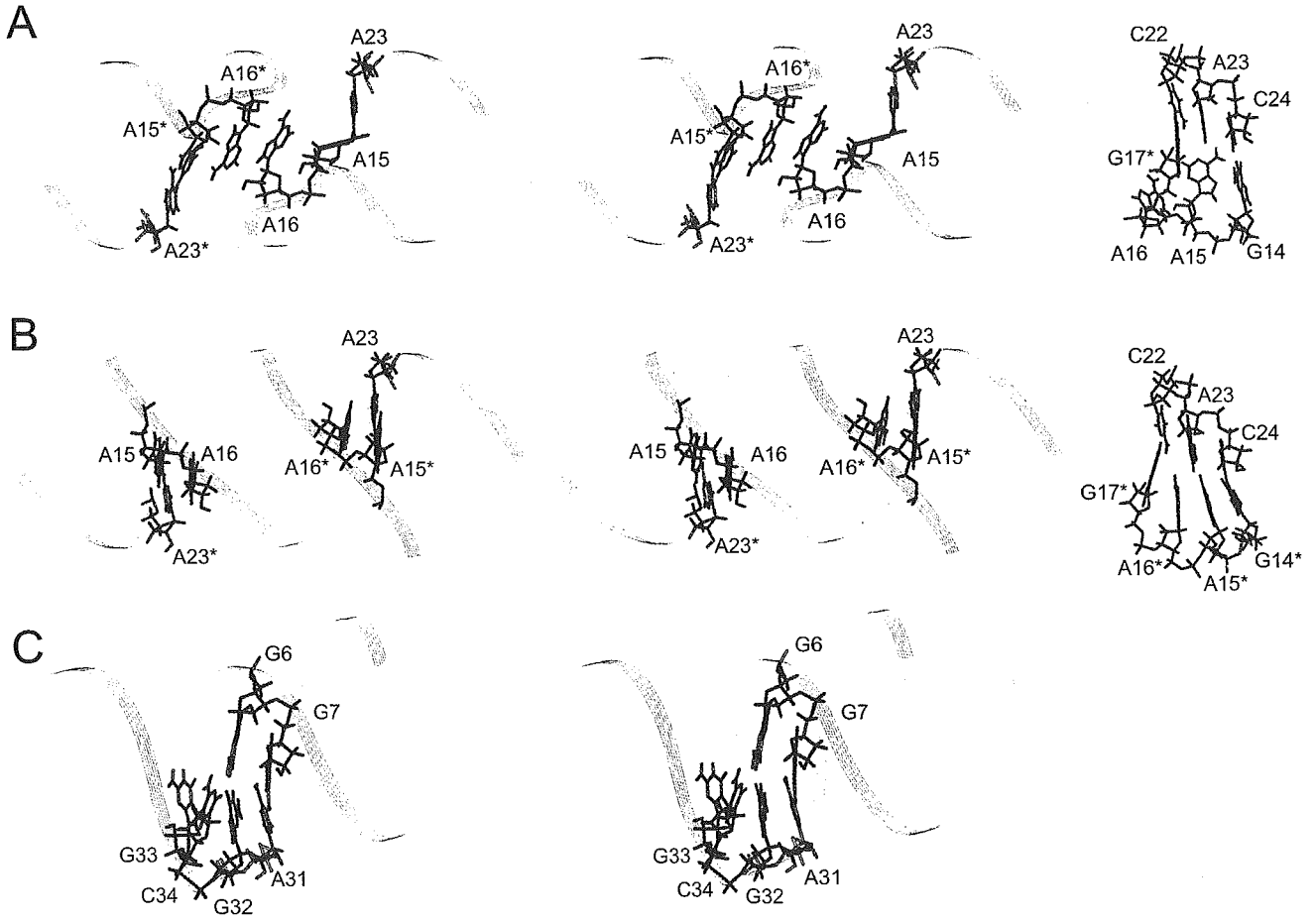

Fig. 6. **Structures of the linking regions.** (A) Regions linking the stem and loop in the kissing-loop dimer. The left panels show the positions of A15, A16, and A23 in the entire structure in a stereo view, and the right panels show residues linking the stem and loop. Asterisks indicate residues in the other strand. (B) Regions linking the stem and loop in the extended-duplex dimer. (C) The bulge region linking the two stems.

extended-duplex dimers. Imino proton signals due to U9:A29 and U10:A28 are much broader than other signals in the stem region, and no imino proton signal due to C8:G30 was observed. Thus, the stem between the loop and bulge is destabilized by the bulge region. Our previous experiments also showed that the bulge region is required for the two-step dimerization to adjust the thermal stability of DIS, and Greatorex *et al.* (*25*) also indicated that the flexibility of the bulge region is critical based on the fact that mutations in the bulge region strongly affect the melting temperature, as well as the fact that none of the wild-type sequences in the bulge region that increase the melting temperature is ever found in wild-type viruses. Thus, the conformational conversion from the kissing-loop dimer to the extended-duplex dimer might require two factors, the movement of A16 and the modest stability of the stem caused by the presence of the bulge region.

In the present study, a set of structures corresponding to the initial and final structures of the two-step dimerization of DIS are provided; these structures will promote studies to elucidate the molecular mechanism of the conformational change in the two-step dimerization, including an analysis of the interaction between DIS and NCp7, in addition to the molecular dynamics approach.

Coordinates: The structure has been deposited in the Protein Data Bank (accession code 2D17: the stem-bulge-stem region of bulge34, 2D18: the extended-duplex dimer of loop25, 2D19: the kissing-loop dimer of loop25, 2D1A: the extended-duplex dimer of DIS39 and 2D1B: the kissing-loop dimer of DIS39).

This work was supported by the "Research for the Future" Program (JSPS-RFTF97L00503) from the Japan Society for the Promotion of Science, and, in part, by a Grant-in-Aid for High Technology Research from the Ministry of Education, Science, Sports and Culture, Japan.

REFERENCES

1. Hoglund, S., Ohagen, A., Goncalves, J., Panganiban, A.T., and Gabuzda, D. (1997) Ultrastructure of HIV-1 genomic RNA. *Virology* **233**, 271–279
2. Laughrea, M., Jette, L., Mak, J., Kleiman, L., Liang, C., and Wainberg, M.A. (1997) Mutations in the kissing-loop hairpin of human immunodeficiency virus type 1 reduce viral infectivity as well as genomic RNA packaging and dimerization. *J. Virol.* **71**, 3397–3406
3. Clever, J.L. and Parslow, T.G. (1997) Mutant human immunodeficiency virus type 1 genomes with defects

in RNA dimerization or encapsidation. *J. Virol.* **71**, 3407–3414
4. Paillart, J.C., Berthoux, L., Ottmann, M., Darlix, J.L., Marquet, R., Ehresmann, B., and Ehresmann, C. (1996) A dual role of the putative RNA dimerization initiation site of human immunodeficiency virus type 1 in genomic RNA packaging and proviral DNA synthesis. *J. Virol.* **70**, 8348–8354
5. Laughrea, M. and Jette, L. (1994) A 19-nucleotide sequence upstream of the 5′ major splice donor is part of the dimerization domain of human immunodeficiency virus 1 genomic RNA. *Biochemistry* **33**, 13464–13474
6. Skripkin, E., Paillart, J.C., Marquet, R., Ehresmann, B., and Ehresmann, C. (1994) Identification of the primary site of the human immunodeficiency virus type 1 RNA dimerization *in vitro*. *Proc. Natl. Acad. Sci. USA* **91**, 4945–4949
7. Fu, W. and Rein, A. (1993) Maturation of dimeric viral RNA of Moloney murine leukemia virus. *J. Virol.* **67**, 5443–5449
8. Fu, W., Gorelick, R.J., and Rein, A. (1994) Characterization of human immunodeficiency virus type 1 dimeric RNA from wild-type and protease-defective virions. *J. Virol.* **68**, 5013–5018
9. Laughrea, M. and Jette, L. (1996) Kissing-loop model of HIV-1 genome dimerization: HIV-1 RNAs can assume alternative dimeric forms, and all sequences upstream or downstream of hairpin 248–271 are dispensable for dimer formation. *Biochemistry* **35**, 1589–1598
10. Muriaux, D., Fosse, P., and Paoletti, J. (1996) A kissing complex together with a stable dimer is involved in the HIV- 1Lai RNA dimerization process *in vitro*. *Biochemistry* **35**, 5075–5082
11. Muriaux, D., Girard, P.M., Bonnet-Mathoniere, B., and Paoletti, J. (1995) Dimerization of HIV-1Lai RNA at low ionic strength. An autocomplementary sequence in the 5′ leader region is evidenced by an antisense oligonucleotide. *J. Biol. Chem.* **270**, 8209–8216
12. Laughrea, M., Shen, N., Jette, L., Darlix, J., Kleiman, L., and Wainberg, M.A. (2001) Role of distal zinc finger of nucleocapsid protein in genomic RNA dimerization of human immunodeficiency virus type 1; No role for the palindrome crowning the R-U5 hairpin. *Virology* **281**, 109–116
13. de Guzman, R.N., Wu, Z.R., Stalling, C.C., Pappalardo, L., Borer, P.N., and Summers, M.F. (1998) Structure of the HIV-1 nucleocapsid protein bound to the SL3 ψ–RNA recognition element. *Science* **279**, 384–388
14. Amarasinghe, G.K., de Guzman, R.N., Turner, B.G., Chancellor, K.J., Wu, Z.R., and Summers, M.F. (2000) NMR structure of the HIV-1 nucleocapsid protein bound to Stem-Loop SL2 of the ψ–RNA packaging signal. Implications for Genome recognition. *J. Mol. Biol.* **301**, 491–511
15. Berkowitz, R., Fisher, J., and Goff, S.P. (1996) RNA packaging. *Curr. Top. Microbiol. Immunol.* **214**, 177–218
16. Darlix, J.L., Lopez-Lastra, M., Mély, Y., and Roques, B. (2003) Nucleocapsid protein chaperoning of nucleic acids at the heart of HIV structure, assembly and cDNA synthesis. In *HIV Sequence Compendium 2002* (Kuiken, C., Foley, B., Freed, E., Hahn, B., Marx, P., McCutchan, F., Mellors, J.W., Wolinsky, S., and Korber, B., eds.) pp. 69–88, Los Alamos National Laboratory, Los Alamos, NM
17. Takahashi, K., Baba, S., Koyanagi, Y., Yamamoto, N., Takaku, H., and Kawai, G. (2001) Two basic regions of NCp7 are sufficient for conformational conversion of HIV-1 dimerization initiation site from kissing-loop dimer to extended-duplex dimer. *J. Biol. Chem.* **276**, 31274–31278
18. Baba, S., Takahashi, K., Koyanagi, Y., Yamamoto, N., Takaku, H., Gorelick, R.J., and Kawai, G. (2003) Role of the Zinc Fingers of HIV-1 Nucleocapsid Protein in Maturation of Genomic RNA. *J. Biochem.* **134**, 637–639
19. Mujeeb, A., Clever, J.L., Billeci, T.M., James, T.L., and Parslow, T.G. (1998) Structure of the dimer initiation complex of HIV-1 genomic RNA. *Nat. Struct. Biol.* **5**, 432–436
20. Ennifar, E., Walter, P., Ehresmann, B., Ehresmann, C., and Dumas, P. (2001) Crystal Structures of Coaxially-Stacked Kissing Complexes of the HIV-1 RNA Dimerization Initiation Site. *Nat. Struct. Biol.* **8**, 1064–1068
21. Girard, F., Barbault, F., Gouyette, C., Huynh-Dinh, T., Paoletti, J., and Lancelot, G. (1999) Dimer Initiation Sequence of HIV-1Lai Genomic RNA: NMR Solution Structure of the Extended Duplex. *J. Biomol. Struct. Dyn.* **16**, 1145–1157
22. Mujeeb, A., Parslow, T.G., Zarrinpar, A., Das, C., and James, T.L. (1999) NMR structure of the mature dimer initiation complex of HIV-1 genomic RNA. *FEBS Lett.* **458**, 387–392
23. Ennifar, E., Yusupov, M., Walter, P., Marquet, R., Ehresmann, B., Ehresmann, C., and Dumas, P. (1999) The crystal structure of the dimerization initiation site of genomic HIV-1 RNA reveals an extended duplex with two adenine bulges. *Structure Fold Des.* **7**, 1439–1449
24. Ennifar, E., Walter, P., and Dumas, P. (2003) A Crystallographic Study of the Binding of 13 Metal Ions to Two Related RNA Duplexes. *Nucleic Acids Res.* **31**, 2671–2682
25. Greatorex, J., Gallego, J., Varani, G., and Lever, A. (2002) Structure and Stability of Wild-Type and Mutant RNA Internal Loops from the SL-1 Domain of the HIV-1 Packaging Signal. *J.Mol.Biol.* **322**, 543–557
26. Lawrence, D.C., Stover, C.C., Noznitsky, J., Wu, Z., and Summers, M. F. (2003) Structure of the Intact Stem and Bulge of HIV-1 Psi-RNA Stem-Loop Sl1. *J. Mol. Biol.* **326**, 529–542
27. Yuan, Y., Kerwood, D.J., Paoletti, A.C., Shubsda, M.F., and Borer, P.N. (2003) Stem of SL1 RNA in HIV-1: structure and nucleocapsid protein binding for a 1 × 3 internal loop. *Biochemistry* **42**, 5259–5269
28. Shen, N., Jette, L., Liang, C., Wainberg, M.A., and Laughrea, M. (2000) Impact of human immunodeficiency virus type 1 RNA dimerization on viral infectivity and of stem-loop B on RNA dimerization and reverse transcription and dissociation of dimerization from packaging. *J. Virol.* **74**, 5729–5735
29. Takahashi, K.I., Baba, S., Chattopadhyay, P., Koyanagi, Y., Yamamoto, N., Takaku, H., and Kawai, G. (2000) Structural requirement for the two-step dimerization of human immunodeficiency virus type 1 genome. *RNA* **6**, 96–102
30. Varani, G., Aboul-era, F., and Allain, F.H.-T. (1996) NMR investigation of RNA structure. *Prog. NMR Spect.* **29**, 51–127
31. Takahashi, K., Baba, S., Hayashi, S., Koyanagi, Y., Yamamoto, N., Takaku, H., and Kawai, G. (2000) NMR analysis on intra- and inter-molecular stems in the dimerization initiation site of the HIV-1 genome. *J. Biochem.* **127**, 681–639
32. St.Louis, D.C., Gotte, D., Sanders-Buell, E., Ritchey, D.W., Salminen, M.O., Carr, J.K., and McCutchan, F.E. (1998) Infectious molecular clones with the nonhomologous dimer initiation sequences found in different subtypes of human immunodeficiency virus type 1 can recombine and initiate a spreading infection in vitro. *J. Virol.* **72**, 3991–3998
33. Weixlbaumer, A., Werner, A., Flamm, C., Westhof, E., and Schroeder, R. (2004) Determination of thermodynamic parameters for HIV DIS type loop-loop kissing complexes. *Nucleic Acids Res.* **32**, 5126–5133
34. Dardel, R., Marguet, R., Ehresmann, C., Ehresmann, B., and Blanquet, S. (1998) Solution studies of the dimerization initiation site of HIV-1 genomic RNA. *Nucleic Acids Res.* **26**, 3567–3571

Ku80 autoantigen as a cellular coreceptor for human parvovirus B19 infection

Yasuhiko Munakata, Takako Saito-Ito, Keiko Kumura-Ishii, Jie Huang, Takao Kodera, Tomonori Ishii, Yasuhiko Hirabayashi, Yoshio Koyanagi, and Takeshi Sasaki

Human parvovirus B19 (B19) infects human erythroid cells expressing P antigen. However, some cell lines that were positive for P antigen failed to bind B19, whereas some cell lines had an ability to bind B19 despite undetectable expression of P antigen. We here demonstrate that B19 specifically binds with Ku80 autoantigen on the cell surface. Furthermore, transfection of HeLa cells with the gene of Ku80 enabled the binding of B19 and allowed its entry into cells. Moreover, reduction of cell-surface expression of Ku80 in KU812Ep6 cells, which was a high-sensitive cell line for B19 infection, by short interfering RNA for Ku80 resulted in the marked inhibition of B19 binding in KU812Ep6 cells. Although Ku80 originally has been described as a nuclear protein, human bone marrow erythroid cells with glycophorin A or CD36, B cells with CD20, or T cells with CD3 were all positive for cell-surface expression of Ku80. B19 infection of KU812Ep6 cells and bone marrow cells was inhibited in the presence of anti-Ku80 antibody. Our data suggest that Ku80 functions as a novel coreceptor for B19 infection, and this finding may provide an explanation for the pathologic immunity associated with B19 infection. (Blood. 2005;106: 3449-3456)

Introduction

Human parvovirus B19 (B19) infects erythroid-lineage cells through P antigen and causes various clinical symptoms such as erythema infectiosum, anemia, polyarthritis, or fetal hydrops in humans.[1,2] The cellular receptor for B19 infection has been regarded as blood group P antigen based on the failure of B19 infection in a patient with an hereditary defect of P antigen.[3] However, the target cells of B19 may be not be exclusively P-antigen–positive erythroid-lineage cells, as illustrated by the poor relationship between P antigen expression levels and the efficiency of B19 infection[4] or the failure of B19 binding to globoside.[5] Recently, Weigel-Kelley et al described the role of $\alpha5\beta1$ integrin as the cellular coreceptor for B19 infection.[6] The notion that B19 receptor is not solely P antigen may be compatible with clinical findings that B19 has been detected in mononuclear cells of blood or tonsils with acute or prolonged B19 infection.[7,8] Also, following B19 infection, the numbers of peripheral blood lymphocytes may decrease despite undetectable levels of P antigen on their cell surface.[9,10] Finally, autoimmune-like phenomena including antinuclear antibodies, rheumatoid factors, or antiphospholipid antibodies are often associated with B19 infection,[8,11] and the levels of tumor necrosis factor α (TNF-α) and interferon γ (IFN-γ) secreted from macrophages or T cells are elevated during acute or prolonged B19 infection.[12] Clinical studies have shown that B19 DNA can be amplified from joint samples by polymerase chain reaction (PCR),[13,14] and infective B19 was detected in the articular lesions of patients with rheumatoid arthritis. B19 transcripts and B19 protein viral protein 1 (VP1) were also present in T cells, B cells, macrophages, and follicular dendritic cells.[14] The cellular mechanism that may allow B19 binding and its entry into nonerythroid cells has not been elucidated. In the present study, we explored a putative receptor for B19 that was distinct from P antigen.

Materials and methods

Cells

Macrophage cell lines U937, urinary bladder carcinoma cell line T24, colon cancer cell line SW620, renal adenocarcinoma cell line ACHN, and HeLa cells were provided by the Cell Resource Center for Biomedical Research, Institute of Development, Aging and Cancer, Tohoku University (Sendai, Japan). Human erythroid cell line KU812Ep6[15] was provided by E. Miyagawa (Institute of Fuji Rebio, Tokyo, Japan). T-cell line H9 was purchased from American Type Culture Collection (Manassas, VA). Bone marrow samples were obtained from the volunteers who gave informed consent for the use of their samples for our study. Informed consent was provided in accordance with the Declaration of Helsinki.

Human parvovirus B19

Serum from patient 1 with acute B19 infection was used as the source for B19 in the in vitro infection study. The serum contained 2.5×10^{14} copies of B19-DNA per milliliter but was negative for IgM and IgG anti-B19 antibodies.[16] B19 was purified using cellulose hollow fiber, was provided by Dr. K. Yamaguchi,[17] and used as an antigen for enzyme-linked immunosorbent assay (ELISA).

From the Department of Rheumatology and Hematology, and Department of Virology, Tohoku University Graduate School of Medicine, Sendai, Japan.

Submitted February 8, 2005; accepted July 5, 2005. Prepublished online as *Blood* First Edition Paper, August 2, 2005; DOI 10.1182/blood-2005-02-0536.

Supported by a Grant-in-Aid for Scientific Research (A) from the Ministry of Education, Science, Sports and Culture in Japan.

Y.M. and T.S.-I. designed with research, performed research, and wrote the paper; K.K.-I., J.H., T.K., and T.I. performed research; Y.H. analyzed data; and Y.K. and T.S. designed research.

Y.M. and T.S.-I. contributed equally to this work.

Reprints: Yasuhiko Munakata, Department of Rheumatology and Hematology, Tohoku University Graduate School of Medicine, 1-1 Seiryo-cho, Aoba-ku, Sendai 980-8574, Japan; e-mail: mnkt@mail.tains.tohoku.ac.jp.

The publication costs of this article were defrayed in part by page charge payment. Therefore, and solely to indicate this fact, this article is hereby marked "advertisement" in accordance with 18 U.S.C. section 1734.

Recombinant human parvovirus B19 empty capsid protein

Recombinant human parvovirus B19 empty capsid protein (rB19ECP), prepared as described previously,[18] was kindly provided by K. Kamata at Denka Seiken (Tokyo, Japan). rB19ECP was composed of VP1 and VP2 at a ratio of 5:95, respectively.

Antibodies

Monoclonal anti-Ku80 antibodies that recognized N-terminus (amino acids 3-22) or C-terminus of Ku80 (amino acids 610-705) were purchased from Oncogene (Boston, MA) and BD Biosciences (San Jose, CA), respectively. PAR3 is a mouse monoclonal antibody recognizing VP2, which shared with VP1 of B19.[19,20] 1F5 is a mouse monoclonal antibody with anti-idiotypic activity to an anti-DNA antibody,[21] which was used as a control for flow cytometry analysis. GL4, a rabbit polyclonal antigloboside antibody (IgG and IgM), was purchased from Matreya (State College, PA). Monoclonal anti–α5 and anti–β1 integrin antibodies were purchased from Chemicon (Temecula. CA). Other monoclonal antibodies were purchased from BD Biosciences.

In vitro infection of B19

Cells (2×10^6) in 0.5 mL RPMI were infected with B19 containing serum from 1 (diluted at 2×10^{11} copies of B19 DNA/mL) for 30 minutes on ice and washed extensively 3 times with phosphate-buffered saline (PBS), pH 7.2, for evaluation of B19 adsorption. To study B19 replication, the prepared cells in 3 mL RPMI containing 10% fetal bovine serum (FBS) were further incubated at 37°C for 48 hours in a 5% CO_2 humidified atmosphere, followed by 3 extensive washes with PBS and then evaluated for B19 protein and B19 DNA.

Protein precipitation and purification of precipitated protein

Cell-surface protein of H9 cells was labeled with sulfo-NHS esters of biotin (Pierce, Rockford, IL), followed by protein precipitation. H9 cells were treated with Nonidet P-40 lysis buffer (1% Nonidet P-40, 140 mM NaCl, 1 mM phenylmethylsulfonyl fluoride [PMSF], 5 mM EDTA [ethylenediaminetetraacetic acid], 50 mM Tris [tris(hydroxymethyl)aminomethane)–HCl, pH 7.4) and immunoprecipitated with rB19ECP- or bovine serum albumin (BSA)–conjugated cyanogen bromide (CNBr)–Sepharose (Amersham Bioscience, Piscataway, NJ). The precipitated samples were separated under denaturing conditions in a 7.5% sodium dodecyl sulfate–polyacrylamide gel electrophoresis (SDS-PAGE) gel, followed by electrotransfer to a polyvinylidene difluoride (PVDF) membrane. Protein was detected with enhanced chemiluminescence (ECL) Western blotting detection system (Amersham Biosciences) and visualized by LAS-1000 (Fujifilm, Tokyo, Japan). A crude membrane fraction of H9 cells (1×10^{11}) was prepared and solubilized in 1% Nonidet P-40 lysis buffer. The fraction was then precipitated with rB19ECP-conjugated CNBr-Sepharose for 16 hours at 4°C, and the precipitated proteins were separated by SDS-PAGE followed by Coomassie blue staining. Protein sequencing was carried out by Toray Research Center (Kamakura, Japan).

Flow cytometry analysis

Cells were suspended in 100 μL 1% BSA-PBS and incubated with 5 μg/mL test antibodies on ice for 30 minutes. Cells were then washed 3 times with PBS. Cells that required secondary antibodies for detection were further incubated with fluorescein isothiocyanate (FITC)–conjugated goat anti–mouse IgG (or FITC-conjugated anti–rabbit IgG for the GL4 primary antibody; Sigma, St Louis, MO) at 1:200 on ice for 30 minutes. Cells were washed 3 times with PBS before flow cytometry analysis (Becton Dickinson, San Jose, CA). For the detection of Ku80 on the cell surface of bone marrow cells, cells were first reacted with 5 μg/mL anti-Ku80 antibody followed by an incubation with FITC-conjugated anti–mouse IgG antibody. After being washed, cells were reacted with the cell-lineage–specific antibodies (anti–glycophorin A, anti-CD3, anti-CD20, anti-CD56, anti-CD14, or anti-CD36 antibodies) conjugated with phycoerythrin (PE; BD Biosciences) according to the manufacturer's instruction.

In the in vitro infection study, B19-infected cells were fixed with 4% paraformaldehyde followed by permeabilization with SAP buffer (0.1% saponin, 0.05% NaN_3 in Hanks balanced salt solution). Next, cells were incubated with PAR3 at a concentration of 5 mg/mL on ice for 30 minutes, followed by the same procedure as described.

ELISA and quantitative PCR

ELISA was carried out by using rB19ECP-fixed microwells (Denka Seiken). The basic protocol for ELISA and quantitative PCR for measuring B19-DNA was performed as described before.[15,16]

Preparation of cell fraction from B19-infected cells

Cells (6×10^5) were infected with B19 for 30 minutes on ice. Following three washes with PBS, pH 7.2, DNA was extracted from 2×10^5 cells to measure adsorbed B19. The remaining 4×10^5 cells were further incubated for 30 minutes at 37°C, followed by 3 washes with PBS, pH 4.5. To obtain cytoplasm fractions of B19-infected cells, cells were treated with lysis buffer A (100 mM Tris-HCl, pH 7.5, 1% Triton X-100, 5 mM EDTA, 50 mM NaCl, and 100 μM PMSF), and centrifuged. Then, DNA was extracted from the supernatant to measure B19-DNA in cytoplasm. The pellets were washed with lysis buffer A 3 times and treated with lysis buffer B (100 mM Tris-HCl, pH 7.5, 1% Triton X-100, 5 mM EDTA, 500 mM NaCl, and 100 μM PMSF). Following centrifugation, DNA was extracted from the supernatant to measure B19-DNA in nuclei.

Transfection

Five micrograms of expression vector pcD[22] containing pKu80 was used for the transfection of 1×10^5 HeLa cells, and pcD was used as a vector-only control. Transfection was done using the lipofectin method (Invitrogen, Carlsbad, CA). Transfected HeLa cells were infected with B19 for 30 minutes at 37°C. After being washed 3 times with PBS, pH 7.2, cells were collected with 5 mM EDTA-PBS, and B19 was detected by confocal microscopy analysis. Transfected HeLa cells were incubated with 1 μg/mL biotinylated rB19ECP in the presence of 5 μg/mL inhibitor antibodies for 30 minutes at 37°C. After being washed 3 times with PBS, pH 7.2, cells were collected with 5 mM EDTA-PBS, and rB19ECP or Ku80 was detected by confocal microscopy analysis.

RNA interference of K80 in KU812Ep6

The short interfering RNA (siRNA) for Ku80 was synthesized targeting the sequence between nucleotide numbers 130 and 148: 5′-CAAGCAAA-GAAGGUGAUAAdTdT-3′ (sense), 3′-dTdTGUUCGUUUCUUCCAC-UAUU-5′ (antisense). Disordered siRNA of scrambled nucleotide sequence, used as negative control, was 5′-GCGCGCUUUGUAGGAUUCG-dTdT-3′ (sense), 3′-dTdTCGCGCGAAACAUCCUAAGC-5′ (antisense). Synthesized siRNA (200 nM) was transfected to 1×10^6 KU812Ep6 cells by Cell Line Nucleofector Kit V (Amaxa, Gaithersburg, MD) according to the manufacturer's instructions. Transfected cells were subjected to flow cytometry analysis and in vitro infection study of B19, after 48 hours of incubation.

Detection of B19 in HeLa cells by confocal laser microscopy

Cells were grown on glass microslides and fixed with 4% paraformaldehyde in PBS for 10 minutes at room temperature. Cells were blocked with PBS containing 10% FBS for 30 minutes at 4°C, followed by incubation with mouse monoclonal anti-B19 antibody PAR3 (10 μg/mL) for 30 minutes at 4°C, then washed with PBS twice, and incubated with FITC-conjugated goat anti–mouse IgG (1:100; Sigma) for 30 minutes at 4°C. To detect localization of Ku80 and rB19ECP, cells on glass microslides were incubated with mouse monoclonal anti-Ku80 antibody (5 μg/mL) for 30 minutes at 4°C, washed with PBS twice, and incubated with tetramethyl isothiocyanate (TRITC)–conjugated goat anti–mouse IgG (1:50; Sigma) for 30 minutes at 4°C; cells were further incubated with avidin-FITC (1:100; Gibco, Carlsbad, CA) for 30 minutes at 4°C for the detection of labeled

rB19ECP. Confocal miscroscopy analysis was performed with a D-ECLIPSE CI (Nikon, Kawasaki, Japan) mounted with 20×/0.50 or 40×/0.75 Plan Fluor dry objective lenses. Excitation at 488 nm from an argon laser and at 543 nm from a helium-neon laser was used. Images were acquired with E2-C1 2.00 software (Nikon) and processed with Adobe Photoshop 7.0.1 (Adobe Systems, San Jose, CA).

Results

Identification of B19-binding protein on the cell surface of nonerythroid cells

To identify a putative receptor for B19, we first checked the expression of P antigen (Figure 1). Flow cytometry analysis revealed that α5β1 integrin[6] was also positive on the surface of all cell lines tested (data not shown). We then studied the binding and replication of B19 in association with the expression of P antigen and α5β1 integrin. Quantitative study for cell-surface binding, B19 DNA replication, and fluorescence-activating cell sorting (FACS) analysis using anti–B19 protein (VP2) antibody PAR3 revealed that B19 binds not only to a P antigen–expressing erythroid cell line KU812Ep6 but also to a macrophage cell line, U937, to a T-cell line, H9, and a renal carcinoma cell line, ACHN, in which P antigen was undetectable on the cell surface. None of the cell lines, T24, SW620, and HeLa, bound B19 despite surface P antigen expression (left column in Figure 1A). FACS analysis at 48 hours after B19 infection revealed 2 types of staining patterns for B19 protein following immunohistochemistry using PAR3: (1) intense staining in KU812Ep6 and (2) weak staining in Ku812Ep6, U937, H9, and ACHN (left column in Figure 1B). Replication of B19 DNA and the synthesis of B19 protein was observed in KU812Ep6, but not in any of the other cells, irrespective of the presence of P antigen (right column in Figure 1A and right column in Figure 1B) or α5β1 integrin.

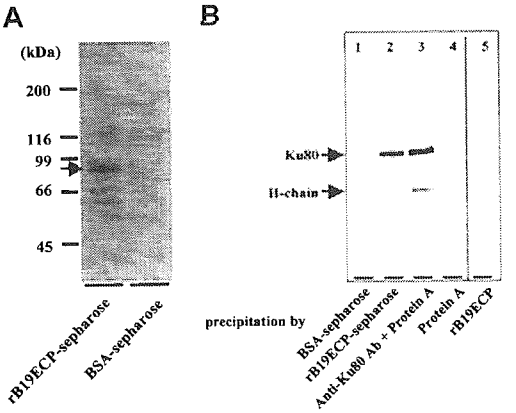

Figure 2. Determination of B19-binding protein on surface of T cell line H9. (A) Isolation of B19-binding protein from H9 surface. Surface proteins H9 of cells were biotinylated. Cell lysate from 1×10^{11} biotinylated H9 cells was mixed with rB19ECP-conjugated Sepharose or with BSA-conjugated Sepharose. Precipitated protein was isolated and reacted with streptavidin–horseradish-peroxidase conjugate on PVDF membranes, followed by the chemiluminescence detection. (B) Western blotting of protein from H9 surface with anti-Ku80 antibody. Lanes 1-4 show cell lysate precipitated with indicated protein or protein-conjugated Sepharose. Lane 5 shows the rB19ECP (1 μg) resolved by electrophoresis under denaturing conditions.

To determine the cell-surface molecule responsible for B19 binding to H9 cells, a recombinant empty capsid protein of B19 (rB19ECP) was used. Biotinylated rB19ECP bound H9 in a dose-dependent manner (data not shown). We then purified the rB19ECP-binding molecule from the cell surface of H9 using rB19ECP-conjugated Sepharose (rB19ECP-Sepharose). The precipitated 80-kDa protein (Figure 2A) was analyzed by matrix-assisted laser desorption ionization-time of flight mass spectrometry. The obtained data were collated and submitted for homology search using the Swiss Prot and NCB Inr databases. The Ku80 autoantigen was identified as the gene product with the highest

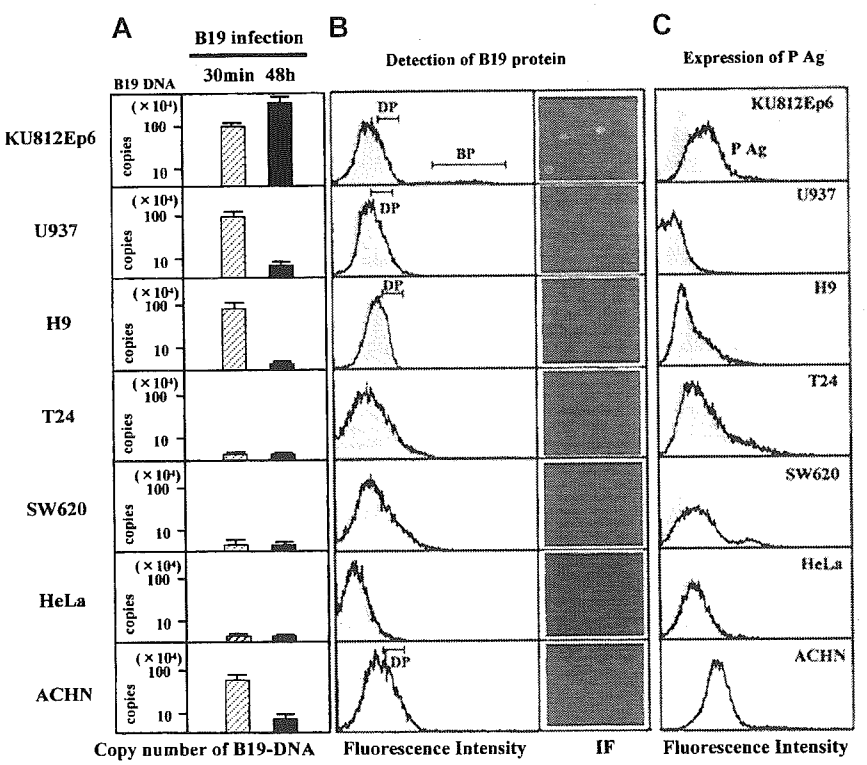

Figure 1. B19 infectivity and expression of P antigen. Each cell line (2×10^6) was inoculated with B19 (1×10^{11} copies of B19 DNA) for 30 minutes at 4°C and washed with PBS, pH 7.2, 3 times. Half of the cells in each group were used for evaluation of B19 adsorption (left column in panel A), and remaining cells in 3 mL RPMI containing 10% FBS were further incubated at 37°C for 48 hours to measure B19 DNA replication (right column in panel A) or to detect B19 protein (B). (A) B19 binding and replication of B19 in various cell lines. B19-infected cells were quantified for B19 DNA as described in "Materials and methods." The left column (▨) is regarded as B19 adsorption, and the right column (■) as B19 replication. The scale for B19 DNA is shown in logarithm. (B) Detection of B19 protein in B19-infected cells. After a 48-hour incubation with B19, the cells were washed 3 times with PBS and they were fixed with 4% paraformaldehyde followed by permeabilization with SAP buffer (0.1% saponin, 0.05% NaN_3 in Hanks balanced salt solution). Then, cells were incubated with PAR3 at a concentration of 5 μg/mL on ice for 30 minutes, followed by an incubation with FITC-conjugated goat anti–mouse IgG. The expression of B19 protein in cytoplasm was analyzed by flow cytometry with PAR3 (line) or isotype-matched antibody 1F5 (shadow; left panel), or by immunofluorescence (IF) staining with PAR3 (right panel). Two types of positive patterns were observed in flow cytometry: dull positive (DP) pattern in KU812Ep6, U937, H9, and ACHN; bright positive (BP) pattern in KU812Ep6. (C) Flow cytometry analysis of P antigen expression on the cell surface. Indicated cells were incubated with antiglobloside antibody, GL4, followed by PE-labeled anti–rabbit IgG. Shadow represents staining using rabbit IgG as a negative control.

homology in both databases. As a confirmation, the rB19ECP-binding 80-kDa protein reacted with anti-Ku80 antibody (Figure 2B). Competitive ELISA further confirmed the specific binding between Ku80 and B19. Biotinylated recombinant Ku80 (rKu80) reacted with rB19ECP fixed to microwells (Figure 3A); the binding was selectively inhibited by unlabeled rKu80 but not by recombinant Ku70 (rKu70), globoside, or recombinant soluble CD26 (sCD26)[23] (Figure 3B). This binding was also inhibited in the presence of native B19 particles from infected patients (Figure 3C). Two anti-Ku80 antibodies significantly inhibited the binding of biotinylated rKu80 and rB19ECP, whereas anti-Ku70 antibody or anti-CD106 antibody failed to inhibit the binding (Figure 3D).

Ku80 participates in B19 binding and subsequent entry

We next investigated whether Ku80 would participate in B19 binding on the cell surface and facilitate B19 entry. KU812Ep6, U937, H9, and ACHN cells efficiently bound B19 (Figure 1A) and all of these cells clearly expressed Ku80 on their surface (Figure 4A). On the other hand, Ku80 was undetectable on T24, SW620, and HeLa cells, and no binding of B19 occurred (Figures 4A and 1A). An in vitro infection experiment demonstrated efficient replication of B19 DNA in KU812Ep6 cells that expressed both Ku80 and P antigen. B19 failed to amplify itself in U937, H9, and ACHN cells, which express Ku80 but no detectable levels of P antigen on the cell surface (Figures 1 and 4A). T24, SW620, and HeLa cells were nonpermissive for B19 infection although they expressed P antigen (Figure 1) and α5β1 integrin.

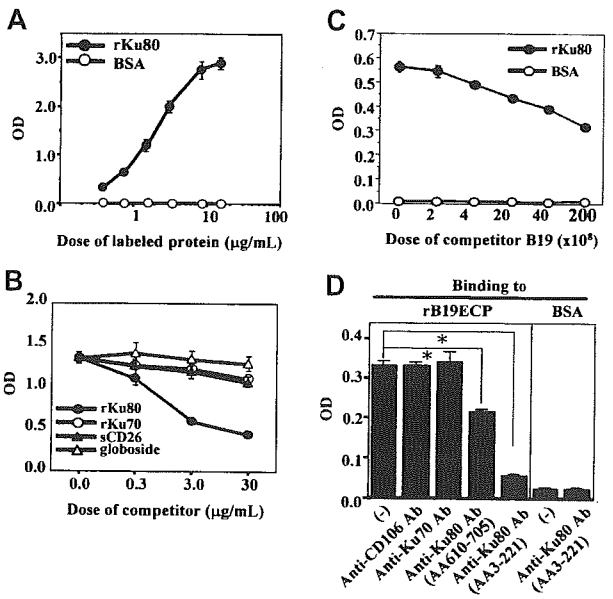

Figure 3. Specific binding of rB19ECP to Ku80. (A) Specific binding of Ku80 to rB19ECP. Indicated concentration of biotinylated rKu80 or biotinylated BSA was reacted with rB19ECP fixed to 96 microwells and detected by ELISA. (B) Competitive ELISA for rB19ECP binding to rKu80. Biotinylated rKu80 (2 μg/mL) was reacted with rB19ECP fixed to wells in the presence of indicated doses of unlabeled rKu80, rKu70, sCD26, or globoside. (C) Inhibition of rB19ECP binding to rKu80 by purified B19. Biotinylated rKu80 (1 μg/mL) was added to rB19ECP fixed to wells in the presence of B19 that was purified from B19+ serum with repeated microfiltration. Doses of B19 are expressed as copy numbers of B19 DNA. (D) Inhibition of rB19ECP binding to rKu80 by anti-Ku80 antibodies. Binding of biotinylated rKu80 or biotinylated BSA to rB19ECP fixed to wells was measured in the presence of isotype-matched mouse monoclonal antibodies as indicated.

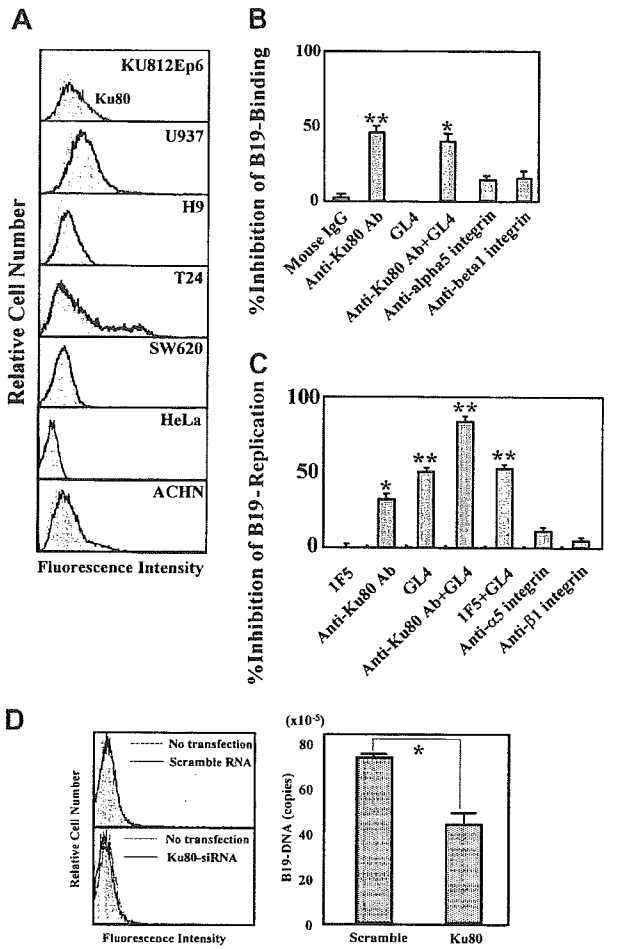

Figure 4. Role of Ku80 in B19 infection in vitro. (A) Ku80 expression on cell surface. The indicated cell lines were reacted with 5 μg/mL mouse monoclonal anti-Ku80 antibody (line) or 5 μg/mL isotype-matched mouse monoclonal antibody 1F5 (shadow), followed by FITC-labeled anti–mouse IgG antibodies. Cells were washed with PBS, and cell-surface expression of Ku80 was analyzed by flow cytometry. (B) Blocking of B19 adsorption by anti-Ku80 antibody or antiglobuside antibody. KU812Ep6 cells (2×10^6) were infected with B19 (2×10^{11} copies of B19 DNA) on ice for 30 minutes in the presence of the indicated antibodies (5 μg/mL) and extensively washed with PBS 3 times. To activate α5β1 integrin, anti-integrin antibodies were used in the presence of divalent ions (1 mM Mn^{2+}, 1 mM Mg^{2+}). B19 DNA in each group was quantified by quantitative PCR. The blocking ability of B19 binding by each antibody was expressed as percent decrease of B19-DNA in each group compared to that in antibody-untreated cells. $^{**}P < .01$, $^{*}P < .05$ by Student *t* test. (C) Blocking of B19 replication by anti-Ku80 antibody or antiglobuside antibody. KU812Ep6 cells were infected with B19 and washed as described. Cells were further incubated for 48 hours at 37°C and washed with PBS 3 times before the quantitative study of B19 DNA. To activate α5β1 integrin, anti-integrin antibodies were used in the presence of divalent ions (1 mM Mn^{2+}, 1 mM Mg^{2+}). The blocking ability of B19 replication by each antibody was expressed as described. $^{**}P < .01$, $^{*}P < .05$ by Student *t* test. (D) RNA interference of Ku80 in KU812Ep6 cells. Cell-surface expression of Ku80 was examined by flow cytometry in scramble RNA or siRNA of Ku80-transfected KU812Ep6 cells (left panel). KU812Ep6 cells treated with indicated RNA were reacted with 5 μg/mL mouse monoclonal anti-Ku80 antibody or 5 μg/mL isotype-matched mouse monoclonal antibody 1F5 (shadow), followed by FITC-labeled anti–mouse IgG antibodies. B19 association of siRNA-transfected KU812Ep6 cells was evaluated by quantitative PCR (right panel). Sample DNA was prepared from extensively washed scramble RNA or siRNA of Ku80-transfected KU812Ep6 cells after 2 hours of incubation with B19. $^{*}P < .01$ by Student *t* test.

Ku80 functions as a coreceptor for B19 infection together with P antigen

We then performed an inhibition test for B19 infection of KU812Ep6 cells using antibodies against Ku80, P antigen, α5β1 integrin. Anti-Ku80 antibody inhibited B19 binding, whereas anti-P antibody, GL4, did not inhibit B19 binding. Anti–α5 and anti–β1

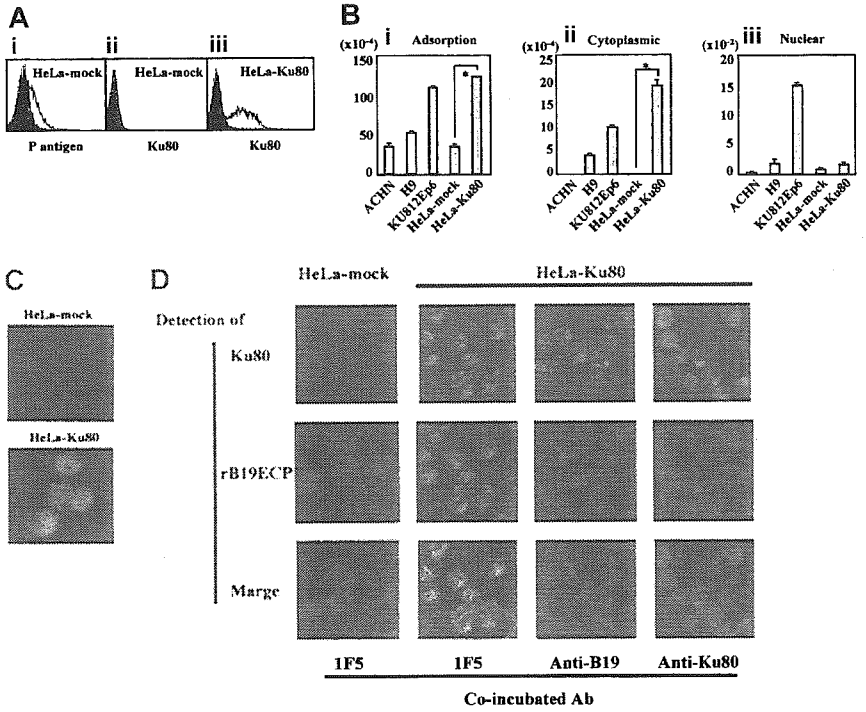

Figure 5. Transfection of Ku80 to HeLa cells. (A) Expression of Ku80 on HeLa cells transfected with pKu80. Ku80 cDNA was inserted to expression plasmid pcD and the resulted pKu80 was transfected to HeLa cells (HeLa-Ku80) using lipofectin. Empty pcD was used for a mock transfection (HeLa-mock). The transfected cells (2×10^5) were incubated with 5 μg/mL of each antibody, anti-Ku80 antibody (ii,iii), GL4 (A1), or isotype-matched mouse monoclonal antibodies or rabbit serum (shadow), and then analyzed for the expression of P antigen or Ku80 on the cell surface. Figures show HeLa-mock expressed P antigen but not Ku antigen on the surface (i,ii), whereas HeLa-Ku80 expressed Ku80 (iii). (B) Increased binding and viral entry of B19 in HeLa-Ku80. The indicated cells (6×10^5) were infected with B19 (2×10^{11} copies of B19 DNA) for 30 minutes on ice. After washing cells 3 times with PBS, pH 7.2, DNA was extracted from 2×10^5 cells. Remaining cells were further incubated for 30 minutes at 37°C. After washing cells 3 times with PBS, pH 4.5, a cytoplasmic and nuclear fraction was prepared, and then DNA was extracted from each fraction. Prepared DNA was subjected to a quantitative PCR to quantify B19 DNA. $^*P < .01$ by Student *t* test. (C) B19 infection to HeLa-Ku80. HeLa-mock or HeLa-Ku80 cells (2×10^5) were infected with B19 (2×10^{11} copies of B19 DNA) for 30 minutes at 37°C. After being washed 3 times with PBS, cells were collected with 5 mM EDTA-PBS, pH 7.2, fixed with 4% paraformaldehyde and reacted with PAR3, followed by FITC-labeled anti–mouse IgG antibody as a secondary antibody. Thus prepared cells were then subjected to a confocal microscope analysis. The panel represents B19 entered into HeLa-Ku80. (D) Colocalization of rB19ECP and Ku80. HeLa-mock or HeLa-Ku80 (2×10^5) cells were incubated with biotinylated rB19ECP (1 μg/mL) in the presence of 5 μg/mL inhibitor antibody indicated for 30 minutes at 37°C. After being washed 3 times with PBS, pH 7.2, cells were collected with 5 mM EDTA-PBS, and rB19ECP or Ku80 was detected by confocal microscopy analysis. Ku80 was detected by anti-Ku80 antibody followed by TRITC-labeled anti–mouse IgG antibody as a secondary antibody. Detection of biotinylated rB19ECP was done by avidin-FITC as described in "Materials and methods."

integrin antibodies caused a slight inhibition of B19 binding (Figure 4B). Both anti-Ku80 antibody and GL4 also inhibited B19 replication in KU812Ep6 cells. The simultaneous presence of both antibodies more strongly inhibited the replication of B19 DNA (Figure 4C). Presence of anti–α5 and anti–β1 integrin antibodies caused only a slight inhibition of B19 replication (Figure 4C). In other experiments, KU812Ep6 cells were treated with siRNA against Ku80 and then tested for the replication of B19 at B19 infection study. The results revealed the suppression of B19 binding to the KU812Ep6 cells with reduced expression of Ku80 (Figure 4D).

The role of Ku80 as a coreceptor for B19 infection was also supported by a transfection experiment using HeLa cells that were nonpermissive for B19 infection. Figure 5A shows that the surface of Ku80-transfected HeLa cells (HeLa-Ku80) became positive for Ku80 expression and binding of B19 to the cells was significantly enhanced (Figure 5B). Quantitative analysis of B19 DNA (Figure 5B) and confocal laser microscopy (Figure 5C) confirmed that B19 DNA and B19 protein were present in the cytoplasmic fraction of HeLa-Ku80 cells 30 minutes after infection, similar to Ku812Ep6. Furthermore, a coincubation experiment of rB19ECP and HeLa-Ku80 revealed the colocalization of rB19ECP and Ku80 in the cytoplasm or membrane (or both) of HeLa-Ku80 (Figure 5D). Moreover, association of rB19ECP and HeLa-Ku80 was apparently inhibited by the presence of anti-B19 antibody or anti-Ku80 antibody (Figure 5D).

Ku80 is expressed on the surface of bone marrow cells

Because Ku80 is known as a nuclear protein, it is important to determine whether or not Ku80 is expressed on the cell-surface in vivo. Ku80 was not detected on the cell surface of peripheral blood mononuclear cells (data not shown). We then examined cell-surface expression of Ku80 in bone marrow cells because bone marrow cells are potential targets of B19 infection. Flow cytometry analysis of bone marrow cells demonstrated that Ku80 was highly expressed on the cell surface of erythroid progenitor cells expressing glycophorin A as well as on the surface of immune cells such as $CD20^+$, $CD3^+$, or $CD14^+$ cells in bone marrow (Figure 6A). A small portion (5.6%) of $CD36^+$ bone marrow cells, which may be permissive to B19 infection,[23] were also positive for the expression of Ku80 on the cell surface (Figure 6B). B19 binding to bone marrow cells was inhibited in the presence of anti-Ku80 antibody at B19 infection in vitro (data not shown). Figure 7 shows that the replication of B19 in bone marrow cells was significantly inhibited in the presence of anti-Ku80 antibody or GL4. The inhibition rate of B19 replication in the presence of both anti-Ku80 antibody and GL4 was similar to that in the presence of GL4.

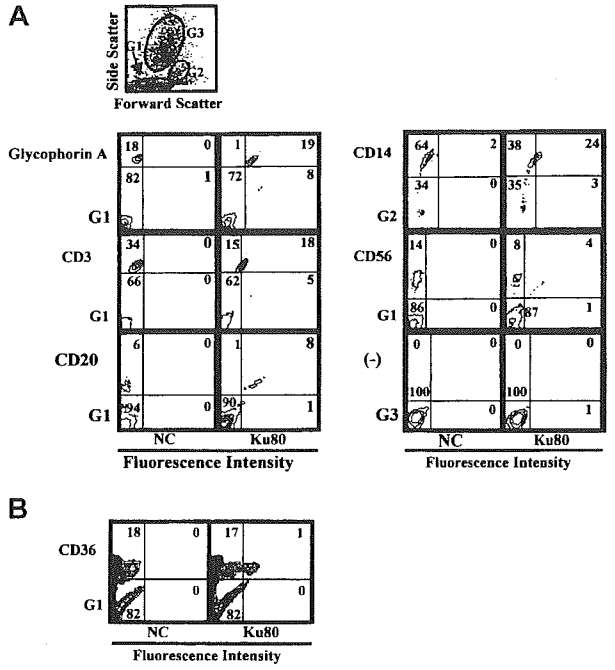

Figure 6. Cell-surface expression of Ku80 in human bone marrow cells. Flow cytometry analysis of Ku80 expression on the cell surface. Bone marrow cells were reacted with indicated antibodies and anti-Ku80 antibody as described in "Materials and methods," and then the expression of surface molecules was analyzed. Prior to the study, each sample had been analyzed by the scattered plot. The results showed that the glycophorin A^+, $CD3^+$, $CD20^+$, $CD56^+$, or $CD36^+$ cells were scattered in gate 1 (G1), and $CD14^+$ cells in gate 2 (G2), and that there were no glycophorin A^+, $CD3^+$, $CD20^+$, $CD56^+$, or $CD36^+$ cells in gate 3 (G3). Then the expression of Ku80 on cell surface in gated cells was analyzed. The gate used in each experiment is shown at left-lower side of each plot. (A) Gates used in the experiment and detection of Ku80 on the surface of various cell lineages. (B) Detection of Ku80 on the surface of $CD36^+$ bone marrow cells.

Discussion

The presented data implicate Ku80 as a coreceptor involved in B19 infection. U937, H9, and ACHN cells expressing Ku80 showed B19 binding, but some cells with P antigen failed to bind B19 unless these cells expressed Ku80 on their surface. A marked increase in B19 binding in Ku80-transfected HeLa cells and the inhibition of B19 infectivity by anti-Ku80 antibody or siRNA to Ku80 suggests a Ku80-dependent B19 interaction with the targeted cells. Specific inhibition of B19 binding by anti-Ku80 antibody that recognized the N-terminus of the Ku80 protein suggests that B19 interacts with specific sites of Ku80 on the cell surface. Further, Epstein-Barr virus or hepatitis virus C failed to bind either to Ku80-expressing HeLa or U937 cells (data not shown). These results suggest that Ku80 is one of the specific receptors for B19 infection.

Ku is a heterodimeric DNA-binding protein consisting of a 70-kDa (Ku70) and an 80-kDa (Ku80) subunit and was originally identified as a nuclear antigen recognized by autoantibodies in patients with systemic lupus erythematosus and scleroderma.[25] Ku has a central role in multiple nuclear processes, including DNA repair, chromosome maintenance, transcription regulation, and V(D)J recombination. Ku is abundant in the nucleus, consistent with its function as a DNA-protein kinase (DNA-PK).[26,27] However, recent studies have shown cytoplasm or surface localization of Ku in various types of cells, including of leukemia, multiple myeloma, and tumor cell lines. Ku is a component of the DNA-PK complex in membrane rafts of mammalian cells.[26] Although the role of surface Ku80 has not been well clarified,[28] signal transduction and Ku80 are coupled in both B and T cells,[25,28,29] and localization of the DNA-PK complex in lipid rafts suggests a putative role in the signal transduction pathway following ionizing radiation.[26] It was recently reported that Ku interacts with metalloproteinase 9 at the cell surface of highly invasive hematopoietic cells of normal and tumor cell origin, and Ku80/MMP-9 interaction at the cell membrane may result in contribution to the invasion of tumor cells through regulation of extracellular matrix remodelling.[30] Further, the membrane form of Ku, whose expression is induced at hypoxia, mediates cell adhesion of plasma cells,[30-32] indicating a role for Ku as an adhesion receptor for fibronectin.[33] The present study showed that Ku80 is positive on the surface of $CD3^+$ cells, $CD20^+$ cells, $CD14^+$ cells, glycophorin A^+ cells, and $CD36^+$ cells from bone marrow where B19 infection is permissive.

We have discovered a novel role of Ku80 as a cellular receptor in B19 infection. Anti-Ku80 antibody, however, did not cause complete inhibition of B19 infection, whereas pretreatment with anti-Ku80 antibody together with GL4 strongly inhibited B19 infectivity in KU812Ep6 cells and human bone marrow cells, showing the necessity of P antigen as a receptor. A recent report showed that $\alpha5\beta1$ integrin has a role in B19 entry into host cells,[6] and KU812Ep6, U937, H9, ACHN, and HeLa cells all expressed $\alpha5\beta1$ integrin on their surface (data not shown). However, B19 entry into U937- and H9-expressing Ku80 and $\alpha5\beta1$ integrin or HeLa cells with P antigen and $\alpha5\beta1$ integrin was insufficient or negative (Figures 1 and 5B). B19 entry was marked in KU812Ep6 cells or Ku80-HeLa cells that expressed Ku80, P antigen, and $\alpha5\beta1$ integrin on their surface, showing the necessity of P antigen for efficient binding and the virus entry afterward. Anti–$\alpha5$ and anti–$\beta1$ integrin antibodies, which inhibited the entry of B19 into K562 cells,[6] caused a slight inhibition of B19 binding as well as B19 replication in KU812Ep6, supporting the participation of $\alpha5\beta1$ integrin in B19 infection. We are currently investigating the precise mechanism of the interaction among B19-related receptors such as P antigen, Ku80, and $\alpha5\beta1$ integrin in association with the following signal transduction in B19-infected cells.

The use of multiple receptors for entry into cells has been observed frequently in virus infection, such as by α herpesviruses, HHV-8 or HIV.[34,35] We have shown that B19 uses at least 2 receptors, Ku80 and P antigen, in the process of infection. Ku80

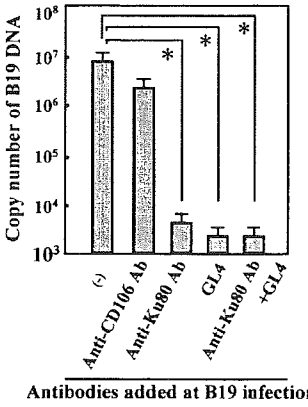

Figure 7. Blocking of B19 infection of bone marrow cells by anti-Ku80 antibody or antiglioboside antibody. Bone marrow cells (2×10^6) were infected with B19 (2×10^{11} copies of B19 DNA) with the indicated antibodies and evaluated for quantity of B19 DNA as described. Anti-CD106 antibody was a mouse monoclonal antibody used as a negative control. The differences in the results between control (−) and other samples were statistically analyzed. $^*P < .01$ by Student *t* test.

may function as an efficient B19-capturing molecule on the cell surface and may also contribute to B19 entry into cells; markedly enhanced entry of B19 in Ku80-HeLa cells (Figure 5C-D) suggests that Ku80 mediates efficient B19 entry in cooperation with P antigen and probably with α5β1 integrin.[6] Although Ku80 can interact with Epstein-Barr virus protein in the nucleus,[36] this study is the first to show the use of Ku80 antigen as a cellular receptor for virus infection. Despite marked entry of B19, synthesis of B19 protein was unsuccessful in Ku80-HeLa cells, but was possible only in erythroid cell lines, indicating that unknown intracellular factors may be required for B19 replication in the targeted cells.[37,38]

Ku80 is not found in circulating mononuclear cells from healthy volunteers but is positive on the surface of B19-binding cells in vivo, such as immune cells in tonsils, erythroblasts, T cells, B cells, macrophages in bone marrow, and immune cells including follicular dendritic cells in rheumatoid joints, indicating the surface expression of Ku antigen may be restricted by environmental conditions. Of interest is that the oxygen levels are markedly low in bone marrow and joints[39-41] compared with that in blood, and surface Ku80 is inducible with hypoxia.[31,32] A recent study suggests the efficiency of B19 infection increases with hypoxia.[42] These studies suggest that surface Ku80 induced with hypoxia may participate in the process of B19 infection of joints and bone marrow.

Ku80 expression on the surface of immune cells in bone marrow in vivo may explain clinical findings associated with B19 infection to nonerythroid cells. Namely, B19 infection often causes a decreased number of leukocytes or lymphocytes in blood during acute B19 infection, as well as increased levels of TNF-α and IFN-γ in blood or rheumatoid joints, and the detection of B19 on T cells, B cells, or macrophages in tonsils, bone marrow, or rheumatoid joints. B19 may infect immune cells in bone marrow or the synovium and persist to lead to secrete an inflammatory cytokine through the activation of AP1 and AP2 by B19 NS1.[43] Stimulation of cellular receptors with B19 may trigger activation of signal cascades in host cells, which may explain why immune cells in acute and prolonged B19 infection or in the joints of rheumatoid arthritis are functionally altered.

Acknowledgments

We are grateful to E. Miyagawa for KU812Ep6, K. Kamata for rB19ECP, T. Mimori for rKu80 and rKu70, C. Morimoto for sCD26, K. Yamaguchi for purified B19, and S. Shibahara for the pKu80.

References

1. Anderson MJ, Jones SE, Fisher-Hoch SP, et al. Human parvovirus, the cause of erythema infectinosum (fifth disease) [letter]? Lancet. 1983;1:1387.
2. Brown KE, Young NS. Parvovirus B19 in human disease. Annu Rev Med. 1997;48:59-67.
3. Brown KE, Anderson SM, Young NS. Erythrocyte P antigen: cellular receptor for B19 parvovirus. Science. 1993;262:114-117.
4. Weigel-Kelly KA, Yoder MC, Srivastava A. Recombinant human parvovirus B19 vectors: erythrocyte P antigen is necessary but not sufficient for successful transduction of human hematopoietic cells. J Virol. 2001;75:4110-4116.
5. Kaufmann B, Baxa U, Chipman PR, Rossmann MG, Modrow S, Seckler R. Parvovirus B19 does not bind to membrane-associated globoside in vitro. Virology. 2005;332:189-198.
6. Weigel-Kelley KA, Yoder MC, Srivastava A. α5β1 integrin as a cellular co-receptor for human parvovirus B19: requirement of functional activation of {beta} 1 integrin for viral entry. Blood. 2003; 102:3927-3933.
7. Wagner AD, Goronzy JJ, Matteson EL, Weyand CM. Systemic monocyte and T cell activation in a patient with human parvovirus B19 infection. Mayo Clin Proc. 1995;70:261-265.
8. Murai C, Munakata Y, Takahashi Y, et al. Rheumatoid arthritis after human parvovirus B19 infection. Ann Rheum Dis. 1999;58:130-132.
9. Anderson MJ, Higgins PG, Davis LR, et al. Experimental parvovirus infection in humans. J Infect Dis. 1985;152:257-265.
10. Barlow GD, Mckendrick MW. Parvovirus B19 causing leucopenia and neutropenia in a healthy adult. J Infect. 2000;40:192-195.
11. Nesher G, Osborn TG, Moore TL. Parvovirus infection mimicking systemic lupus erythematosus. Semin Arthritis Rheum. 1995;24:297-303.
12. Kerr JR, Barah F, Mattey DL, et al. Circulating tumor necrosis factor-α and interferon-γ are detectable during acute and convalent parvovirus B19 infection and are associated with prolonged and chronic fatigue. J Gen Virol. 2001;82:3011-3019.
13. Soderlund M. Persistence of parvovirus B19 DNA in synovial membranes of young patients with and without chronic arthropathy. Lancet. 1997; 349:1063-1065.
14. Takahashi Y, Murai C, Munakata Y, et al. Human parvovirus B19 as a causative agent for rheumatoid arthritis. Proc Natl Acad Sci U S A. 1998;95: 8227-8232.
15. Miyagawa E, Yoshida T, Takahashi H, et al. Infection of the erythroid cell line, KU812Ep6 with human parvovirus B19 and its application to titration of B19 infectivity. J Virol Methods. 1999;83:45-54.
16. Saito T, Munakata Y, Fu Y, et al. Evaluation of anti-parvovirus B19 activity in sera by assay using quantitative polymerase chain reaction. J Virol Methods. 2003;107:81-87.
17. Yamaguchi K, Miyagawa E, Dan M, Miyazaki T, Ikeda H. Cellulose hollowfibers (BMMS) used in the filter membrane can trap human parvovirus B19 [abstract]. Electron Microsc. 2002;2:115.
18. Kajigaya S, Shimada T, Fujita S, Young NS. Self-assembled B19 parvovirus capsids, produced in a baculovirus system, are antigenically and immunogenically similar to native virions. Proc Natl Acad Sci U S A. 1991;88:4646-4650.
19. Yaegashi N, Tada K, Shiraishi H, Ishii T, Nagata K, Sugamura K. Characterization of monoclonal antibodies against human parvovirus B19. Microbiol Immunol. 1989;33:561-567.
20. Brown CS, Jensen T, Meloen RH, et al. Localization of an immunodominant domain on baculovirus produced parvovirus B19 capsids: correlation to a major surface region on the native virus particle. J Virol. 1992;66:6989-6996.
21. Harata N, Sasaki T, Osaki H, et al. Therapeutic treatment of New Zealand mouse disease by a limited number of anti-idiotypic antibodies conjugated with neocarzinostatin. J Clin Invest. 1990; 86:769-776.
22. Okayama H, Berg P. A cDNA cloning vector that permits expression of cDNA inserts in mammalian cells. Mol Cell Biol. 1983;3:280-289.
23. Tanaka T, Duke-Cohen JS, Kameoka J, et al. Enhancement of antigen-induced T-cell proliferation by soluble CD26/dispetidyl peptidase IV. Proc Natl Acad Sci U S A. 1994;91:3082-3086.
24. Morey AL, Fleming KA. Immunophenotyping of fetal haematopoietic cells permissive for human parvovirus B19 replication in vitro. Br J Haematol. 1992;82:302-309.
25. Mimori T, Ohosone Y, Hama N, et al. Isolation and characterization of cDNA encoding the 80-kDa subunit protein of the human autoantigen Ku(p70/p80) recognized by autoantibodies from patients with scleroderma-polymyositis overlap syndrome. Proc Natl Acad Sci U S A. 1990;87: 1777-1781.
26. Adam L, Bandyopadhyay D, Kumar R. Interferon-α signaling promotes nucleus-to-cytoplasmic redistribution of p95Vav, and formation of a multisubunit complex involving Vav, Ku80, and Trk-2. Biochem Biophys Res Commun. 2000;267:692-696.
27. Hector L, Darren G, Guillermo ET. Novel localization of the DNA-PK complex in lipid rafts. J Biol Chem. 2003;278:22136-22143.
28. Prabhakar BS, Allaway GP, Srinivasappa J, Notkins AL. Cell surface expression of the 70-kD component of Ku, a DNA-binding nuclear autoantigen. J Clin Invest. 1990;86:1301-1305.
29. Morio T, Hanissian SH, Bacharier LB, et al. Ku in the cytoplasm associates with CD40 in human B cells and translocates into the nucleus following incubation with IL-4 and anti-CD40 mAb. Immunity. 1999;11:339-348.
30. Monferran S, Paupert J, Dauvillier S, Salles B, Muller C. The membrane form of the DNA repair protein Ku interacts at the cell surface with metalloproteinase 9. EMBO J. 2004;23:3758-3768.
31. Teoh G, Urashima M, Greenfield EA, et al. The 86-kD subunit of Ku autoantigen mediates homotypic and heterotypic adhesion of multiple myeloma cells. J Clin Invest. 1998;101:1379-1388.
32. Lynch EM, Moreland RB, Ginis I, Perrine SP, Faller DV. Hypoxia-activated ligand HAL1/13 is lupus autoantigen Ku80 and mediates lymphoid cell adhesion in vitro. Am J Physiol Cell Physiol. 2001;280:897-911.
33. Sylvie M, Catherine M, Lionel M, Philippe F, Bernard S. The membrane-associated form of the DNA repair protein Ku is involved in cell